Article:

Ye, Q, Luo, Q, Connolly, DP orcid.org/0000-0002-3950-8704 et al. (3 more authors) (2023) The effect of asphaltic support layers on slab track dynamics. Soil Dynamics and Earthquake Engineering, 166. 107771. ISSN 0267-7261

https://doi.org/10.1016/j.soildyn.2023.107771

The effect of asphaltic support layers on slab track dynamics

Qingzhi Ye
School of Civil Engineering, Southwest Jiaotong University, Chengdu 610031, China
Email: qingzhiye@my.swjtu.edu.cn

Qiang Luo
School of Civil Engineering, Southwest Jiaotong University, Chengdu 610031, China
MOE Key Laboratory of High-Speed Railway Engineering, Chengdu 610031, China
Email: lqrock@swjtu.edu.cn

David P. Connolly
Institute for High Speed Rail and System Integration, University of Leeds, Leeds LS2 9JT, UK
Email: D.Connolly@leeds.ac.uk

Tengfei Wang*
School of Civil Engineering, Southwest Jiaotong University, Chengdu 610031, China
MOE Key Laboratory of High-Speed Railway Engineering, Chengdu 610031, China
ORCID: 0000-0003-4079-0687
Email: w@swjtu.edu.cn (*Corresponding author)

Hongwei Xie
School of Civil Engineering, Southwest Jiaotong University, Chengdu 610031, China
Email: hongweixie@my.swjtu.edu.cn

Haibo Ding
School of Civil Engineering, Southwest Jiaotong University, Chengdu 610031, China
Email: haibo.ding@swjtu.edu.cn

Abstract

The deployment of asphaltic support layers (ASLs) within railway track structures has the potential to increase track bending stiffness, assist moisture runoff and provide a platform for track construction. These merits have increased its usage within the rail industry, however the understanding of asphaltic track dynamics during train loading remains limited. Therefore, the primary aim and novelty of this study is the development of new knowledge into the dynamic behavior of concrete slab track systems enhanced with asphaltic underlays. To do so, a numerical simulation approach is used, comprised of two sub-models: 1) a coupled multi-body vehicle–track model, for the purpose of computing wheel/rail forces; and 2) a 3D dynamic finite element track-ground model to simulate stress wave propagation in the sub-structure. The models are validated using both analytical results and field tests, and then used to simulate slab track systems with ASL thicknesses of: 0, 0.05, 0.07, 0.10, and 0.15 m. First the dynamic response at locations both near and far from the track joints are compared to quantify the asphaltic foundation stresses, deflections, accelerations and strains. It is found that stress concentrations occur near the concrete base joints and are an important consideration for ASL design. Next, asphalt concrete durability at 400 km/h line speed is explored considering seasonal temperature variations and it is found that the expected cumulative damage meets serviceability requirements. Finally, the influence of different asphaltic layer thicknesses on reaction modulus is discussed, concluding that the optimal thickness range, considering plastic deformation and construction constraints, is between 0.07 m and 0.10 m.

Keywords: Asphalt concrete; Asphaltic slab track; Vehicle–track coupled dynamics; Dynamic finite element method; Railway asphalt vibration; Railway trackbed

Nomenclature

ASL	Asphalt support layer
AUR	Upper roadbed underneath asphalt support layer
ALR	Lower roadbed in asphalt track foundation
AASHO	American Association of State Highway Officials
ASTB	Asphaltic slab track bed
CRTS III	China Railway Track System III
CRTS II	China Railway Track System II
DOF	Degree of freedom
FEM	Finite element method
HSR	High-speed rail
LR	Lower roadbed in conventional slab tracks (base model)
NMS	Mode numbers of $X_n(x)$ selected for slab modelling
NM	Order number of rail vibration mode
NMB	Mode numbers of $X_n(x)$ selected for concrete base modelling
SBV	Schwellen MIT Bitumen Verguss
VFA	Voids filled with asphalt
WLF	Williams–Landel–Ferry
$[\boldsymbol{C}_v]$	System matrices for damping of vehicle
$[\boldsymbol{K}_v]$	System matrices for stiffness of vehicle
$[\boldsymbol{M}_v]$	System matrices for mass of vehicle
$\{\boldsymbol{P}_{wr}\}$	System force vectors of wheel/rail interaction
$\{\boldsymbol{Z}_v\}$	System displacement vectors of vehicle
$[\varepsilon]$	Threshold elastic strain
$T_n(t)$	Generalized coordinate concerning time t
$X_n(x)$	Mode functions of the slab with x coordinates
$q(t)$	Generalized coordinate for the vertical motion of rail
$\delta(x)$	Dirac function
$\delta Z_j(t)$	Compression at the j^{th} contact point solved by vertical track irregularity, and the wheel and rail displacements
B_s	Width of track slab
B_b	Width of concrete base
C_{BN}	Normal coefficients of spring damping
L_{min}	Distance between two adjacent nodes on a moving load's path.
L_v	Vehicle length
L_b	Length of concrete base
L_c	Bogie spacing
L_s	Length of a single slab
m_s	Track slab mass
M_t	Bogie mass
M_w	Wheelset mass
C_p	Damping of fastener
C_{BT}	Tangential coefficients of spring damping
C_n	Courant number
C_1, C_2	Positive constants in WLF equation
C_s	Shear-wave velocity
C_p	Compressive wave velocity
C_{pz}	Primary suspension damping
C_{sz}	Secondary suspension damping
EI_Y	Rail bending stiffness to the *Y*-axle
E_A	Elastic modulus of asphalt concrete
E_sI_s	Slab bending stiffness
E_bI_b	Concrete base bending stiffness
E_r	Elastic modulus of rail
F_{rs}	Fastener force
G_{wr}	Constant concerning the wheel/rail contact condition
H_b	Height of concrete base
H_s	Height of track slab
I_r	Area moment of rail
J_t	Bogie pitch moment of inertia
J_c	Car body pitch moment of inertia
K_{BT}	Tangential coefficients of spring stiffness
K_{BN}	Normal coefficients of spring stiffness
K_{sz}	Secondary suspension stiffness
K_{30}	Subgrade reaction modulus
k_{sc}	Stiffness per unit length of self-compacting concrete
K_p	Stiffness of fastener
K_{pz}	Primary suspension stiffness
L_t	Axle spacing
l_s	Spacing of fasteners
m_r	Mass per unit length of rail
n_0	Total number of rail fasteners mounted on a single slab
x_{wj}	Position coordinates of the j^{th} wheelset
x_i	Position coordinates of i^{th} fastener point
α_N	Normal correction coefficient
α_T	Tangential correction coefficient
β_n	Frequency coefficient corresponding to $X_n(x)$
λ_{min}	The smallest wave length
ε_r	Tensile strain at the base of ASL
ε_z	Compression strain on the surface of

			roadbed
M_c	Total mass of Car body and dead weight tonnage	ε_{zu}	Compression strain on AUR surface
N_a	Number of load applications required by fatigue damage	ε_{zl}	Compression strain on ALR surface
N_S	Number of loadings with respect to allowable permanent deformation	C	Constant related to VFA
N_i	Number of bogie passages in each season	G	Shear modulus
N_{si}	Allowable number of bogie passages defined for each season related to the deformation-included damage	K	Bulk modulus of the structural layers
N_{ai}	Allowable number of bogie passages defined for each season related to the fatigue damage	N	Total number of rail fasteners
P_0	Design axle load	P	Wheel/rail contact force
R_w	Wheel rolling radius	R	Distance from the boundary to the vibration source
T_{ref}	Reference temperature	T	Temperature
a_T	Shift factor	c	Wave velocity in a medium
c_s	Damping of cement asphalt mortar	β	Correction factor
c_{sc}	Damping per unit length of self-compacting concrete	ρ	Mass density
c_f	Damping per unit length of soil foundation	Δt	Fixed time increment
k_f	Stiffness per unit length of soil foundation		
k_s	Stiffness of cement asphalt mortar layer		

1. Introduction

Ballastless tracks are commonly used on high-speed lines due to their perceived higher performance and reduced maintenance requirements compared to ballasted tracks [1–4]. The subgrade serves as a structural foundation; however, it can be negatively affected by environmental factors (e.g., rainfall and humidity), potentially resulting in frost heave [5,6], mud pumping [7], and other defects [8,9]. Furthermore, the subgrade is typically formed from unbound material with minimal bending stiffness to spread the induced traffic loads.

As a solution, placing asphaltic support layers (ASL) within ballasted and ballastless track systems has recently emerged as an attractive method to reduce substructure deformation by increasing bending stiffness and waterproofing [10–12]. For example, asphalt mixtures, with densely graded aggregates and low air voids (1−3%), can help to provide isolation properties and resistance against water damage [13–15]. Further, during track construction, asphaltic layers provide a high-quality foundation for the operation of heavy plant, thus improving track-bed construction quality. Despite the potential benefits of ASLs, there has been limited scientific research to optimize their usage for railways. Although asphaltic materials are commonplace and well understood in the field of highways, the dynamic loads and lifespans expected in a railway environment are significantly different. For example, highway asphalt pavements lifespans are 15 to 20 years, whereas high-speed rail (HSR) infrastructure is designed to last much longer, up to 100 years [16]. Similarly, highways typically experience relatively low moving load speeds, excited by wavelength ranges that differ significantly from HSR. Further, expansion joints between adjacent track slabs or concrete bases leads to stress concentrations in the track foundations.

Over the last half century, asphalt-based materials have been introduced into existing and newly developed railway systems. The primary application of asphaltic layers has been for ballasted track. For ballasted railway systems, an asphalt underlayment serves as an additional structural layer between the ballast and the subgrade/subballast, with the aim of reducing subgrade deterioration under the combined effects of train loading and water seepage [17]. Early adopters of asphalt included Austria, Italy, America, and Japan, with tests of the technology beginning in the 1960's [18]. The related long-term field evaluations, simulation calculations and recent laboratory tests [19] have shown it to have a positive benefit on trackbed performance.

In addition to ballasted track applications, the asphaltic slab track bed (ASTB) system involves laying asphalt directly under a concrete slab track. Several European countries and Japan first introduced ASTB to construct HSRs and urban transit lines [20]. Varieties of asphaltic slab track beds have been proposed [14], including RA-slab on the Sanyo and Tohoku Shinkansen lines in Japan [21] and Schwellen mit BitumenVerguss (SBV) systems in Germany [22]. However, the widespread application of RA-slabs has been delayed in Japan due to challenges regarding settlement and durability [21]. Further, the SBV system in Germany was also ultimately superseded by system with asphaltic trackbed laid directly below the sleepers [22]. Considering the potential benefits, yet the practical challenges of developing asphaltic slab tracks, currently there is the opportunity to develop new knowledge into the behavior of the technology to overcome the current challenges.

In recent years, dynamic models have been proposed to simulate the interaction of between railway vehicles, track and subgrade [23–25]. When studying subgrade dynamics, the FEM has been proposed to investigate the effect of nonlinear material properties, irregular geometric shapes and structural discontinuities [26]. These include Hall [27] who developed a 3D finite element track-soil model using ABAQUS, which was subject to moving point loads, and the related works have been done by Connolly et al. [28,29], Shih et al. [30,31], Powrie et al. [32] and Varandas et al. [33]. Alternatively, El Kacimi et al. [34] proposed a Fortran based 3D FE code in the time domain, while Galvín and Domínguez [35] proposed a frequency domain solution. Kouroussis et al. [36] combined a vehicle-track coupled system with a full 3D ground model to predict vibrations induced by railway transportation. Auersch [37] and O'Brien & Rizos [38] also coupled a multi-body vehicle system with a 3D FEM-BEM model to evaluate dynamic responses caused by moving trains. Alternatively, 2.5D methods [39–46] and the Thin-Layer Method (TLM) [47–51] have been proposed to take advantage of domain geometry invariances and thus improve computational efficiency. Based on the aforementioned approaches, [52–54] used the finite element method to analyse asphalt railway substructures.

Considering this previous research, two shortcomings are common: 1) Many railway asphalt studies simplify the excitation as a moving point load, thus ignoring train-track interaction, and thus of random track irregularities. This is an important contributor to track dynamics; 2) Most studies have focused on the underlying behaviour of continuous asphalt track structures, thus ignoring the effect of stress concentrations at the longitudinal expansion joints between track slabs and bases. Again, this is an important factor for consideration because this is where the largest dynamic stresses will occur.

Therefore, this work proposes a modified approach that is well-suited to simulating asphaltic railway track, including train-track interaction and expansion joints. It combines a vehicle–track coupled dynamics model with a 3D track–subgrade FE model to simulate the dynamic behavior of ASL within a concrete slab track system. In the coupled dynamic model, random track irregularities are employed as system excitations to calculate the wheel/rail forces. In the FE model, a refined track–subgrade system is proposed, capable of accounting for non-linear material properties, specific geometries and structural discontinuities. A generalized Maxwell model in the form of Prony series is adopted for describing the viscoelasticity of asphalt concrete. The primary novelty of the paper is the use of the model to investigate the dynamic behavior of asphaltic support layers in the presence of train-track interaction and slab joints. To do so, a slab track system model with five different thickness of ASL is simulated. Considering the longitudinal discontinuity of the slab track structure, the stresses, deflections, accelerations, and strains of three joint-dependent locations are analysed. Finally, the durability of asphalt concrete under long-term railway operations is examined, and the implications on ASL design are discussed.

2. Modelling framework

2.1 Modelling overview

Vehicle–track vibrations are primarily induced by the irregular surfaces of wheels and rails. To consider this interaction, a vehicle–track coupled dynamic model is used to calculate the wheel/rail forces. After that, to evaluate the dynamic response of varying subgrades under train passage especially at joint-dependent locations, a track–subgrade model should be capable of accounting for nonlinear material properties, detailed track geometry, structural and discontinuities. To do so, this paper proposes a hybrid modelling strategy solved in the time domain to meet these objectives. The two main modelling steps are shown in Fig. 1:

Vehicle–track sub-model: Calculates the wheel/rail force using vertical vehicle–track coupled dynamics theory. A detailed model is developed for vertical interactions between railway vehicles and tracks. The moving vehicle is modelled as a multi-body system with ten DOF's; the track substructure is simulated as an infinite Euler beam supported on an elastic foundation consisting of the three layers: rail, track slab, and concrete base. The vehicle and the track subsystems are coupled through wheel/rail interaction described using Hertzian non-linear elastic contact theory. Random track irregularities are employed as system excitations via a time−frequency transformation technique.

Track–ground sub-model: Calculates the dynamic response of the track–subgrade system using FEM in the time domain. A 3D FE model is developed considering nonlinear material properties, track geometry, and structural discontinuities. It is used to compute the subgrade's dynamic stress, deflection, and acceleration. Nonreflective boundary conditions facilitate wave propagation towards the far-field area and prevent outward propagating waves from reflecting into the domain of interest. The wheel/rail forces calculated from Vehicle–track sub–model are inputs for the 3D FE track–ground sub–model.

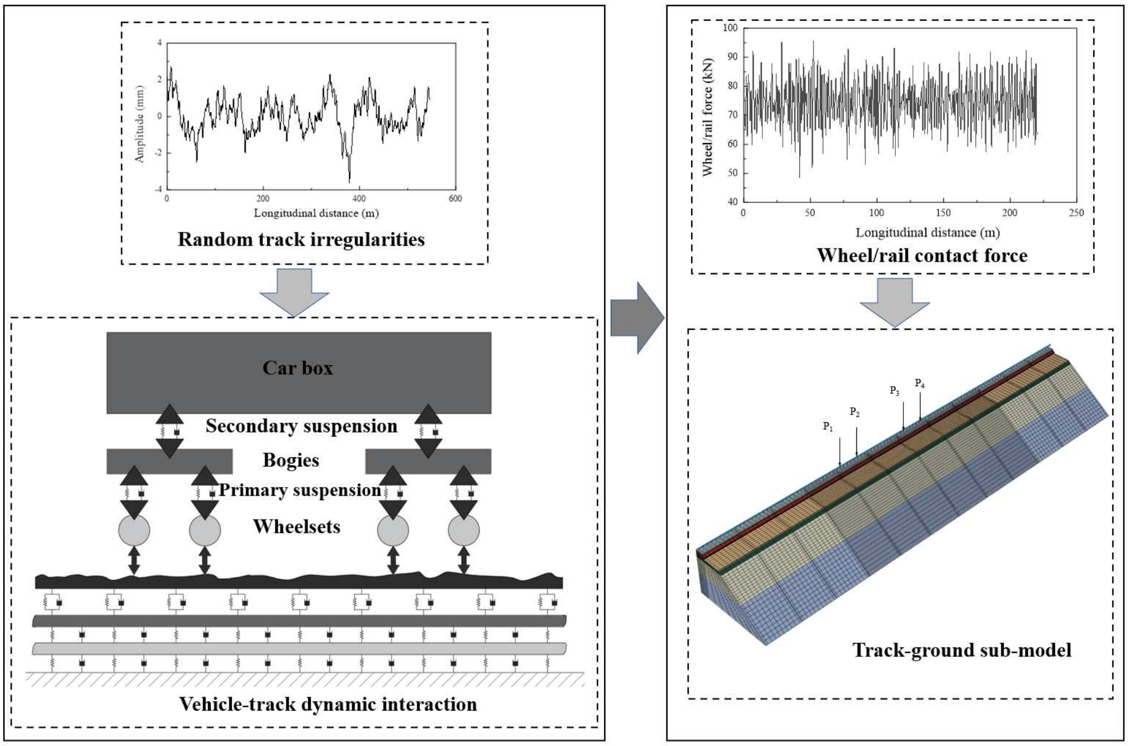

Figure 1. Model overview

2.2 Vertical vehicle–track coupled dynamics

2.2.1 Dynamic equations of motion

A vehicle–track vertically coupled dynamics model incorporating subgrade support is established to characterize the dynamic interactions between the vehicle, slab track structure, and foundation (subgrade), as shown in Fig. 2.

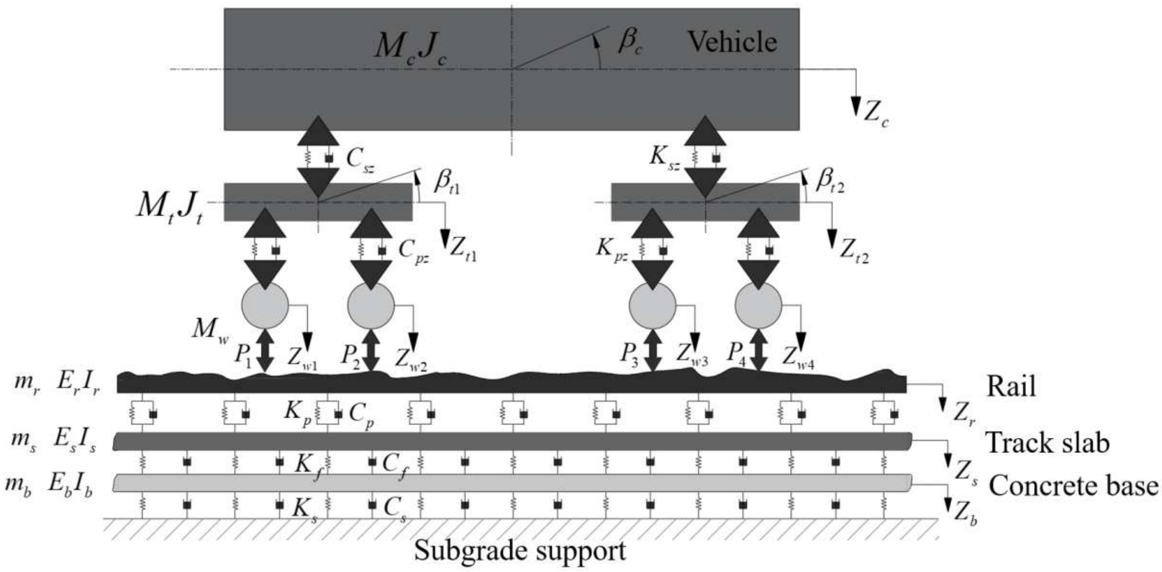

Figure 2. Vertical vehicle–track sub–model considering the subgrade

The vehicle consists of one car body, two bogie frames, and four wheelsets in a four-axle mass-spring-damper system. The primary and secondary suspensions characterized by spring-damping elements are employed to connect the structural components. The bogie frames and car body have two degrees of freedom (DOFs), which means vertical and pitch motions are considered. The wheelsets only have one DOF for vertical motion. The dynamic equation of the vehicle–track interaction model is derived in submatrix form as [23,55]:

$$\begin{bmatrix} \mathrm{M_V} & 0 \\ 0 & \mathrm{M_T} \end{bmatrix} \begin{Bmatrix} \ddot{\mathrm{X}}_\mathrm{V} \\ \ddot{\mathrm{X}}_\mathrm{T} \end{Bmatrix} + \begin{bmatrix} \mathrm{C_V} & 0 \\ 0 & \mathrm{C_T} \end{bmatrix} \begin{Bmatrix} \dot{\mathrm{X}}_\mathrm{V} \\ \dot{\mathrm{X}}_\mathrm{T} \end{Bmatrix} + \begin{bmatrix} \mathrm{K_V} & 0 \\ 0 & \mathrm{K_T} \end{bmatrix} \begin{Bmatrix} \mathrm{X_V} \\ \mathrm{X_T} \end{Bmatrix} = \begin{Bmatrix} \mathrm{F_V} \\ \mathrm{F_T} \end{Bmatrix} \tag{1}$$

where the subscripts ‘V’ and ‘T’ refer to the vehicle sub-system and track sub-system, respectively; [**M**], [**K**] and [**C**] are the system matrices for mass, stiffness, and damping, respectively; {**F**} and {**X**} are the system force and displacement sub-vectors, respectively. Nonlinear contact force is considered for the wheel/rail interactions.

Rail fasteners discretely support a finite-length Bernoulli-Euler beam that represents the rail. Following the Ritz method, the equation for dynamic rail motion can be expressed as [23,55]:

$$\begin{cases} \ddot{q}_k(t) + \dfrac{EI_Y}{m_r}\left(\dfrac{k\pi}{l}\right)^4 q_k(t) = -\sum\limits_{i=1}^{N} F_{rsi}(t) Z_k(x_i) + \sum\limits_{j=1}^{4} p_j(t) Z_k(x_{wj}), k = 1 \sim NM \\ Z_r(x,t) = \sum\limits_{k=1}^{NM} Z_k(x) q_k(t) \end{cases} \tag{2}$$

where the subscript 'k' refers to the fastener; $q\,(t)$ denotes the generalized coordinate for the vertical motion of the rail; EI_Y denotes the rail bending stiffness to the Y-axle; $Z_\mathrm{r}(x, t)$ is the vibration displacement of rail; x_wj and x_i are the position coordinates of the j^th wheelset and i^th fastener point, respectively; P is the wheel/rail contact force; F_rs is the fastener force; N denotes the total number of rail fasteners; and NM represents the order number of the rail vibration mode.

The track slab is modelled as a simply supported Euler–Bernoulli beam on a concrete base, which is in turn supported by a nonlinear viscoelastic foundation. Following the Ritz method, the equations of dynamic motion for the track slab and concrete base are given as [23,55]:

$$\begin{cases} \ddot{T}_{sn}(t)+\frac{E_s I_s L_s \beta_n^4}{m_s}T_{sn}(t)=\sum_{j=1}^{n_0}\frac{F_{rsj}(t)}{m_s}X_n(x_j)-\frac{k_f}{m_s}[L_s T_{sn}(t)-\int_0^{L_s}X_{sn}(t)Z_b(x,t)dx] \\ \qquad -\frac{c_f}{m_s}[L_s\dot{T}_{sn}(t)-\int_0^{L_s}X_{sn}(t)\dot{Z}_b(x,t)dx], n=1\sim NMS \\ Z_b(x,t)=\sum_{n=1}^{NMB}X_{bn}(x)T_{bn}(t) \end{cases} \tag{3}$$

$$\begin{cases} \ddot{T}_{bn}(t)+\frac{E_b I_b L_b \beta_n^4}{m_b}T_{bn}(t)=\frac{k_f}{m_b}[\int_0^{L_b}X_{bn}(t)Z_s(x,t)dx-L_b T_{bn}(t)]+\frac{c_f}{m_b}[\int_0^{L_b}X_{bn}(t)\dot{Z}_s(x,t)dx-L_b\dot{T}_{bn}(t)] \\ \qquad -\frac{k_s}{m_b}L_b T_{sn}(t)-\frac{c_s}{m_b}L_b T_{sn}(t), n=1\sim NMB \\ Z_s(x,t)=\sum_{n=1}^{NMS}X_{sn}(x)T_{sn}(t) \end{cases} \tag{4}$$

where $X_n(x)$ is the mode function of the slab with x coordinates; β_n is the frequency coefficient corresponding to $X_n(x)$; $T_n(t)$ is the generalized coordinate concerning time t; *NMS* and *NMB* are the mode numbers $X_n(x)$ for the slab and concrete base models respectively; $Z_s(x, t)$ and $Z_b(x, t)$ are the vibration displacement of track slab and concrete base, respectively; E_sI_s and E_bI_b are the slab and base bending stiffness respectively; m_s and m_b denote the track slab and concrete base mass respectively; k_f and c_f are the stiffness and damping of the cement asphalt mortar layer between the track slab and base respectively; k_s and c_s are the stiffness and damping of subgrade support respectively; L_s and L_b are the slab and base length respectively; and n_0 is the total number of rail fasteners mounted on a single slab.

2.2.2 Vertical wheel/rail interaction

The vertical wheel/rail contact force determines the wheel/rail dynamic interaction. The derivation of the Hertzian nonlinear contact theory leads to:

$$P_{wrj}(t)=\begin{cases} \left[\frac{1}{G_{wr}}\delta Z_j(t)\right]^{3/2}, & \delta Z_j(t)>0 \\ 0, & \delta Z_j(t)\le 0 \end{cases} \tag{5}$$

where G_{wr} is the constant concerning the wheel/rail contact condition and $\delta Z_j(t)$ is the compression at the j^{th} contact point, which is solved using the vertical track irregularity and the wheel and rail displacements.

2.2.3 Random track irregularities

Vehicle–track vibrations are primarily excited by the irregular surfaces of wheels and rails. Two main types of geometric irregularities exist: 1) specific irregularities, such as the wheel flat, out-of-round wheel, dipped rail joint, and rail corrugation, and 2) random irregularities, such as the roughness on the surfaces of wheels and rails, which influence wheel–rail rolling noise and track geometry. Random track irregularities are inherent on all railway lines and influence the dynamic performance of vehicle and track. This paper focuses on excitations due to random track irregularities.

Random track irregularities can be described using power spectral density (PSD) as a function of spatial frequency, of which there are various formulations. The formulation used in this work is based on TB/T 3352-2014 (National Railway Administration of PRC), which divides the track into different classes to quantify track unevenness [56]. To input the track spectrum into the vehicle–track system, the PSD function is transformed into a rail geometry varying with the track's longitudinal distance (or in the time domain) through a time–frequency transformation technique [57].

2.3 FE Model

A three-dimensional dynamic finite element model of a track structure was built using the commercial software ABAQUS (version 2018) to perform comprehensive analyses of substructure mechanical behaviours in a ballastless track system (CRTS III) under train loading. The train forces were calculated using the coupled dynamics model in the previous computation step and then introduced into the FE model as an excitation.

2.3.1 General description

The ballastless track under consideration was the CRTS III slab track system [16], as shown in Fig. 3. It comprised UIC60 rail, WJ-8B fasteners, P5600 track slab, self-compacting concrete, concrete base, and subgrade. The steel rail is modelled as a 2-node linear beam and the fasteners were deployed at a spacing of 0.63 m [58]. The standard CRTS III P5600 track slab measured 5.6 m in length, 2.5 m in width, and 0.2 m in thickness. The self-compacting concrete layer has the same dimensions as the track slab and is 0.1 meters thick. The concrete base dimensions are 17.0 m long, 3.1 m wide, and 0.3 m thick. The ballastless track system has expansion joints between the slab and concrete base, and the expansion joints are 70 mm wide for the slab and 20 mm wide for the base. As shown in Fig. 3b, a single concrete base supports three track slabs. From the top down, the asphaltic track foundation consists of the ASL, asphaltic upper roadbed (AUR), asphaltic lower roadbed (ALR), and embankment. Note that the total thickness of ASL and AUR is 0.4 m, while the UR thickness is 0.4 m in conventional track foundations [16]. The thicknesses of the ALR and embankment are 2.3 m and 3.0 m, respectively. The subgrade slope gradient was 1:1.5.

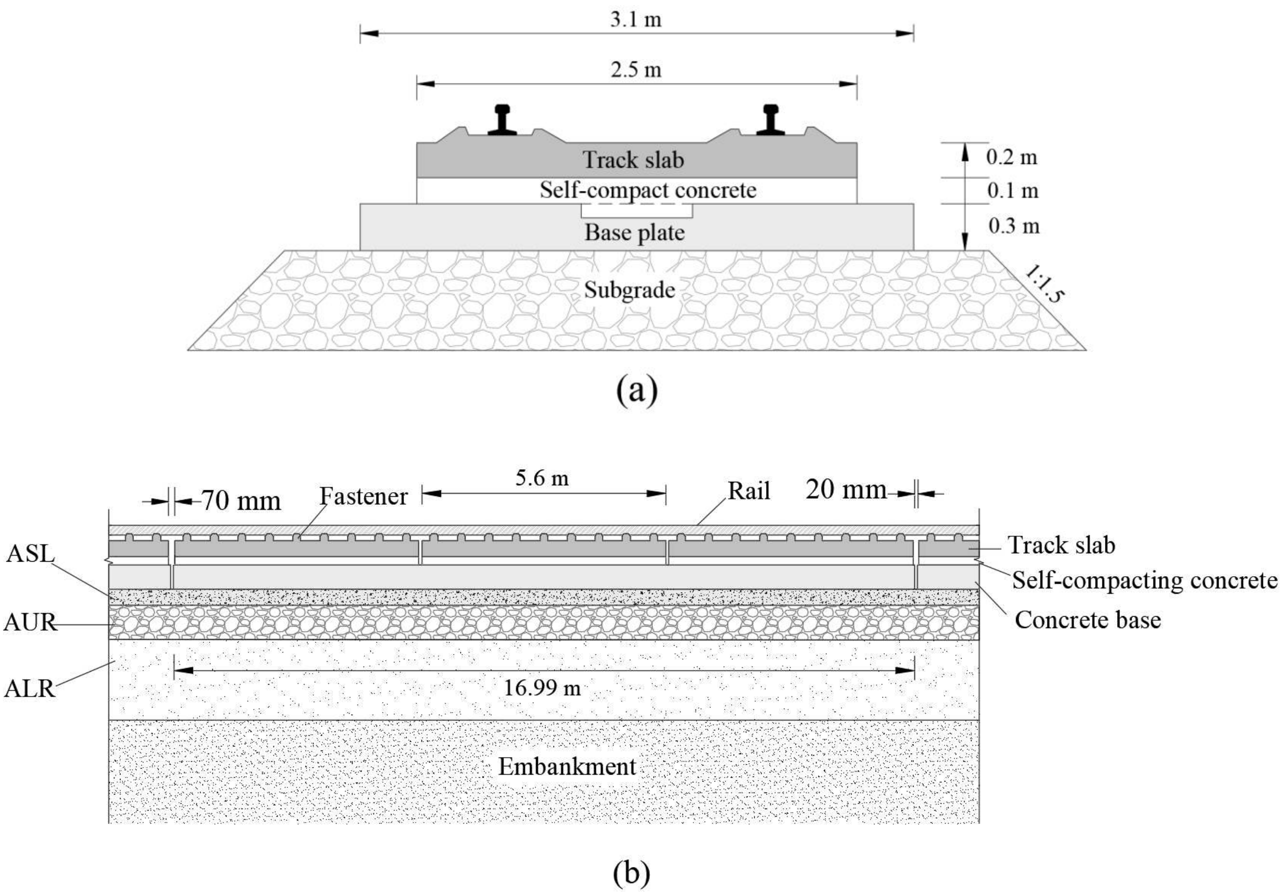

Figure 3. Components of the CRTS III ballastless slab track with expansion joints: (a) cross-section; (b) side view

The developed FE model (Fig. 4) shows four concrete bases totaling 68.04 m. The framework improves computational efficiency by taking the symmetrical half of the slab track system. CARTESIAN connectors simulate fasteners with a vertical dynamic stiffness of 40 kN/mm and damping of 50 kN·s·m^{-1}. The track slab and self-compacting concrete layer are merged into a composite structure by deploying a reinforcing mesh and two rows of door-type modules [59]. A tie constraint is adopted between the track slab and self-compacting concrete layers. In this instance, the tie constraint means that no relative displacement occurs between the two contact surfaces. The self-compacting concrete layer and concrete base are in contact with a coefficient of friction of 0.7 [60]. Because of the low roadbed stiffness and small surface dynamic deformation, a tie constraint is applied to the concrete base and formation. Non-reflective boundary conditions are employed to facilitate wave propagation towards the far-field and prevent the outward propagating waves from reflecting into the computational domain [61].

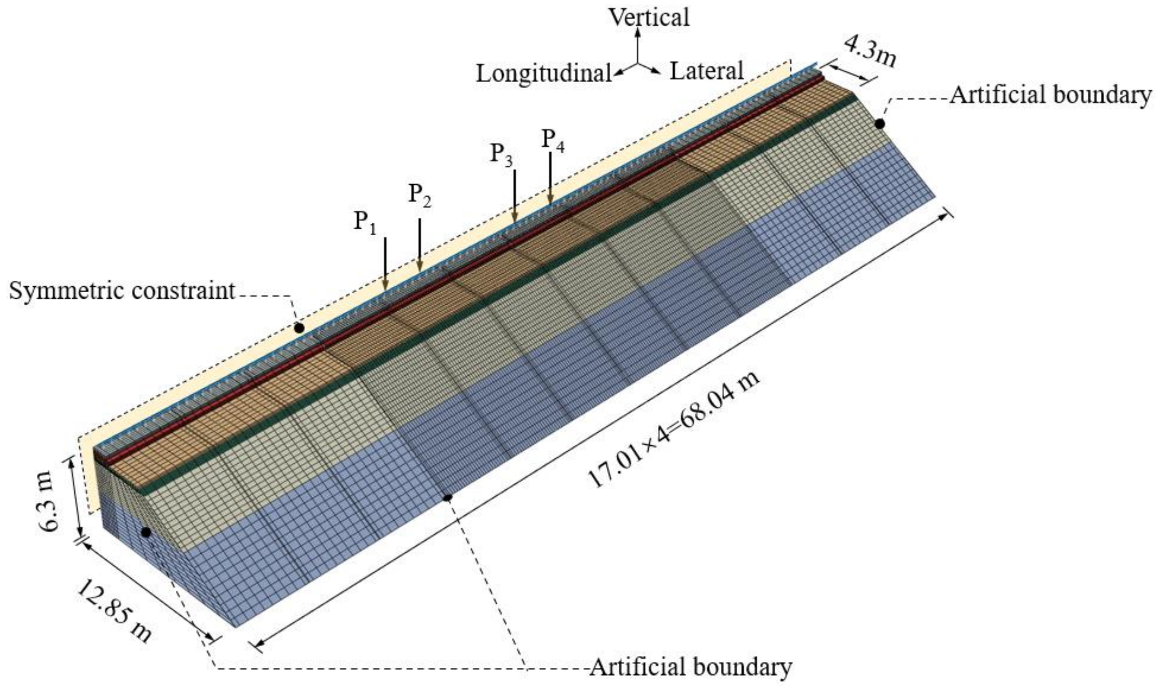

(a)

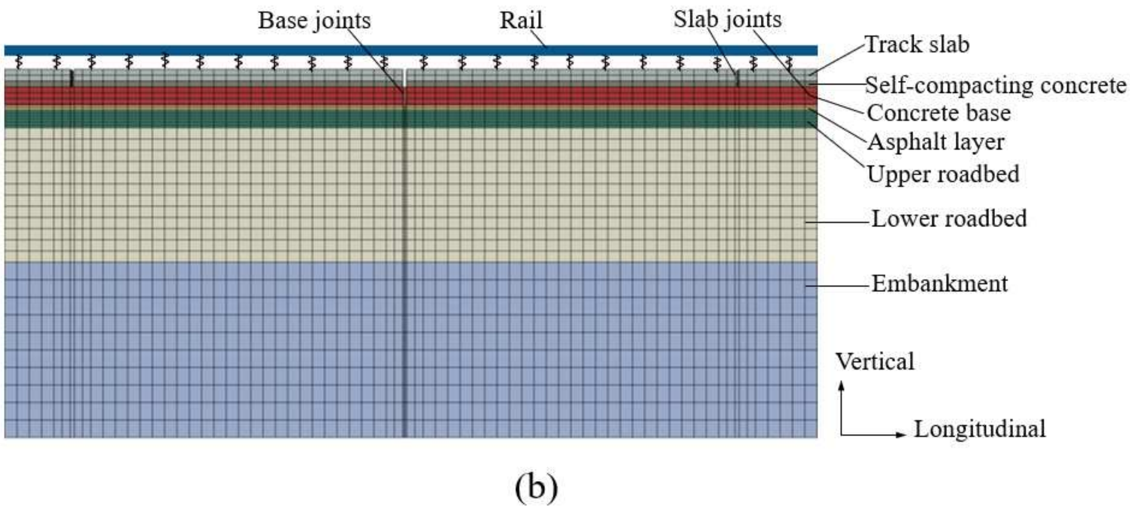

Figure 4. Three-dimensional FE model of the track–subgrade system: (a) general view; (b) elevation view

2.3.2 Moving traffic loads

A double-axle load pattern is used in the loading phase to ensure consistency between the two modelling techniques (Fig. 5). Similar to the coupled dynamics model, the passage of one car is considered in the dynamic FE analysis, corresponding to two bogies and four axles. The wheel/rail contact forces derived from the previous coupled dynamics steps are automatically submitted to a user subroutine DLOAD in ABAQUS, which exerts the concentrated moving force on the rail top based on its spatiotemporal distributions.

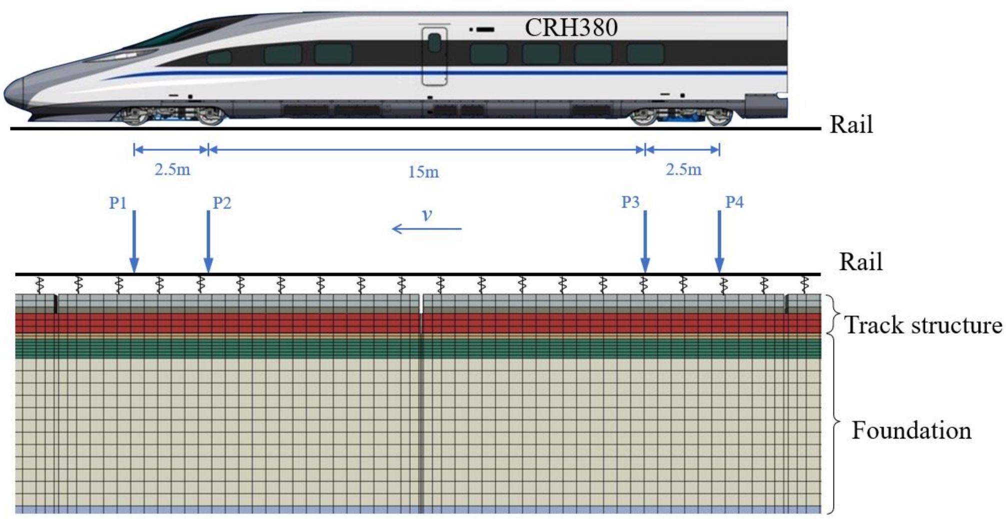

Figure 5. Configuration of moving train loads as inputs in FE analysis

The implementation steps of the dynamic simulation model are displayed in Fig. 6, where the two subsystems are sequentially coupled. The vehicle-track coupled model is used as a first step: it provides the time history of the wheel/rail forces exerted on the rail, which is, in turn, used as inputs in a 3D FE model of the track foundation. The complete process is performed in the time domain.

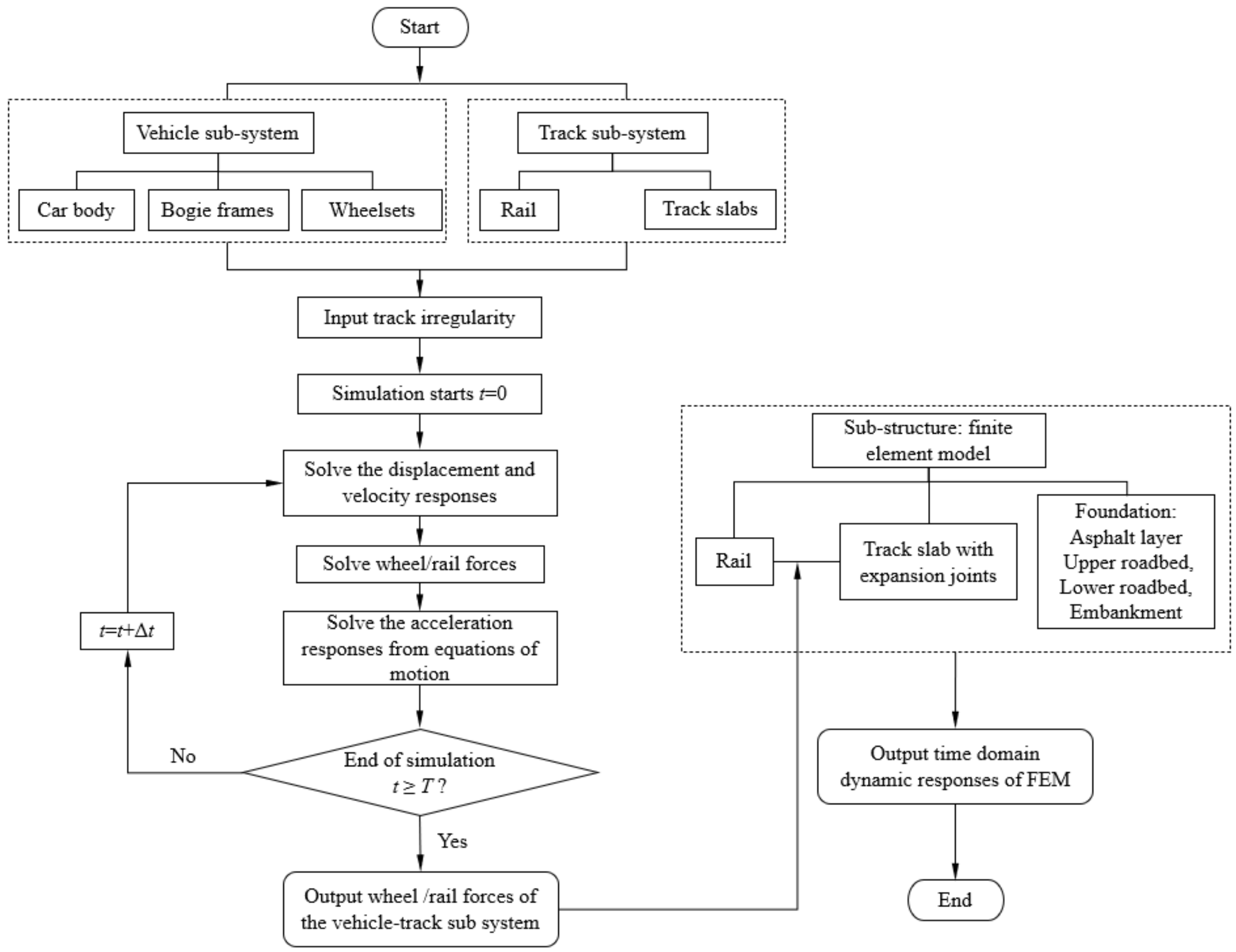

Figure 6. Flowchart for the two-step modelling framework

3. Validation

The following describes two validations used to assess model accuracy. First, the dynamic stress on the subgrade surface of a base model (0 cm thick ASL) is validated by comparing the calculation results against that from Green's function. Then, the deflection and acceleration on the ASL surface are validated using measurement data from in-situ tests performed on the Zhengzhou–Xuzhou line in China.

3.1 Validation 1: Analytical solution without ASL

The two-step modelling framework was validated by comparing the calculation results against those computed using an alternative Green's function solution approach [62,63]. This alternative approach also divided the vehicle–track–subgrade system into two subsystems: the vehicle–rail subsystem and the slab–subgrade subsystem, which were coupled through fastener connections.

To perform the comparison, the CRH2 Electric Multiple Unit running at 300 km/h was considered (Appendix A). Table 1 lists the primary parameters for the ballastless track system. The total length of the rail infrastructure model is 306.18 m, and the vehicle runs a maximum distance of 200 m. The first 263 modes of vibration are used for the rail, track slab, and base, resulting in 789 DOFs in the track model.

Table 1. Calculation parameters for the CRTS III slab track

Components	Parameters	Symbols	Units	Values
Rail	Elastic modulus	E_r	N·m^{-2}	2.1×10^{11}
	Area moment	I_r	m^4	3.09×10^{-5}
	Mass per unit length	m_r	Kg·m^{-1}	60.8
Fastener	Stiffness	K_p	N·m^{-1}	2.5×10^{7}
	Damping	C_p	N· s ·m^{-1}	3.625×10^{4}
	Spacing	l_s	m	0.63
Track slab	Length	L_s	m	5.6
	Width	B_s	m	2.5
	Height	H_s	m	0.3
	Density	ρ_s	Kg·m^{-3}	2,600
Concrete base	Length	L_b	m	16.99
	Width	B_b	m	3.1
	Height	H_b	m	0.3
	Density	ρ_b	Kg·m^{-3}	2,500
Self-compacting concrete	Stiffness per unit length	k_{sc}	N·m^{-2}	1.25×10^{9}
	Damping per unit length	c_{sc}	N·s·m^{-2}	8.3×10^{4}
Subgrade	Stiffness per unit length	k_f	N·m^{-2}	1.7×10^{8}
	Damping per unit length	c_f	N·s·m^{-2}	1.5×10^{5}

According to the power spectral density (PSD) of track irregularities of HSRs specified in TB/T 3352-2014 [56], the PSD function of the ballastless track spectrum of HSRs is piecewise fitted with a power function:

$$S(f)=\frac{A}{f^{k}} \tag{11}$$

where $S(f)$ is the PSD of track irregularities, as shown in Fig. 7; f is the spatial frequency; and A and k are the fit coefficients, as shown in Table 2.

Table 2. Values of A and k for the vertical ballastless track spectrum

Type	A	k
The first segment	1.0544×10^{-5}	3.3891
The second segment	3.5588×10^{-3}	1.9271
The third segment	1.9784×10^{-2}	1.3643
The fourth segment	3.9488×10^{-4}	3.4516

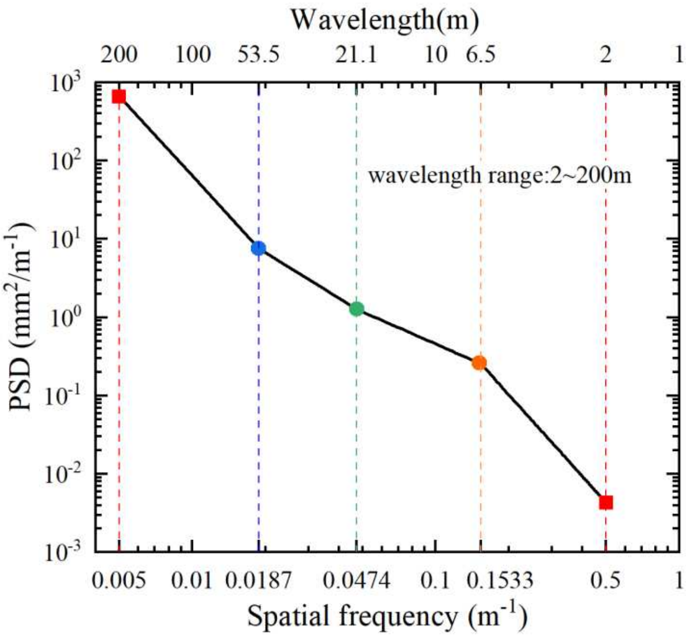

Figure 7. PSD of vertical ballastless track irregularities

The samples of time-domain track irregularities are generated using the inverse Fourier transform method. The wavelength range of the simulation is from 1 to 200 m, and Fig. 8 displays the profile of the generated moderate track irregularities.

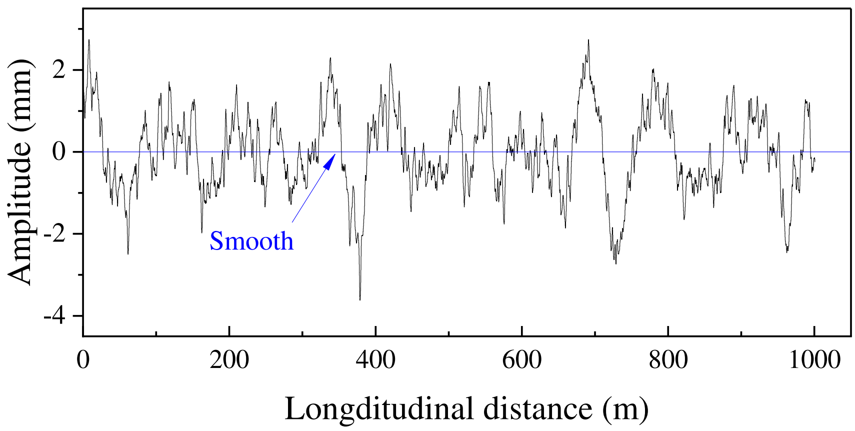

Figure 8. Profile of random track irregularities

The dynamic responses of the slab track structure are obtained based on the vehicle−track vertically coupled dynamics model with random vertical track irregularities. At a speed of 300 km/h, the calculated wheel/rail contact forces considering track irregularity are shown in Fig. 9.

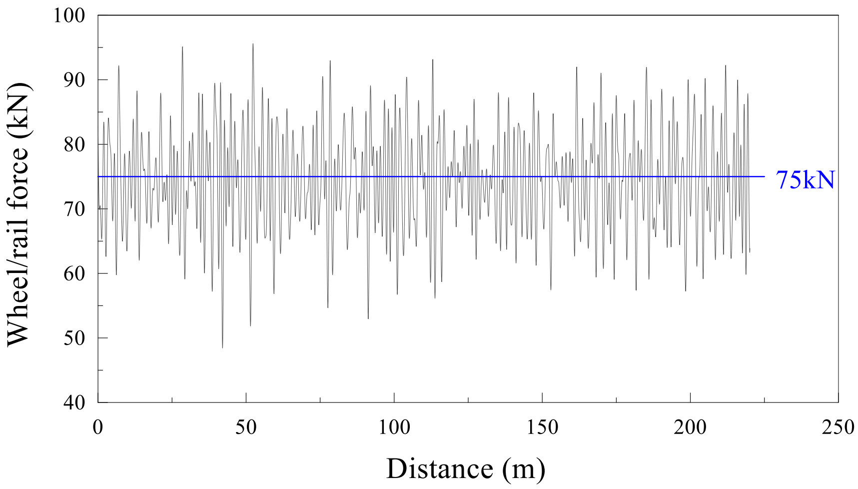

Figure 9. Longitudinal distribution of the wheel/rail contact force (static wheel load =75 kN, running speed = 300 km/h)

Table 3 summarizes the material properties of the track components and formation layers, where the fills are classified per TB10621-2014 [16]. The constitutive relations of the rail, track slab, self-compacting concrete, and concrete base are described using linear elastic models. According to TB10621-2014, the subgrade reaction modulus (K_{30}) values for each layer are 190, 150, and 130 MPa/m. A linear elastic−perfectly plastic model describes the subgrade soil with the Mohr−Coulomb failure criterion, and its elastic modulus is determined per the reported methods [64,65].

Table 3. Material properties of the FE track–subgrade model

Component	Material	Bulk Density (kg/m^3)	Modulus (MPa)	Poisson's ratio	Damping ratio	Friction angle (°)	Cohesion (kPa)
Rail	Steel	7,830	210,000	0.300	0.01	/	/
Track slab	C60 concrete	2,600	36,000	0.167	0.03	/	/
Self-compacting concrete	C40 concrete	2,500	32,500	0.167	0.03	/	/
Concrete base	C40 concrete	2,500	32,500	0.167	0.03	/	/
Upper roadbed	Graded gravel	2,100	228.9	0.300	0.08	28	32
Lower roadbed	Class A/B fill (coarse)	2,050	186.0	0.350	0.07	25	26
Embankment	Class A/B/C fill	2,000	163.5	0.400	0.10	22	25

As shown in Fig. 10, the time histories of the monitored surface stress by the two approaches are comparable. The monitoring point on the roadbed surface shows peak dynamic stresses of 13.8 kPa and 14.1 kPa for the proposed model and Green's function, respectively. Their peak stress difference is less than 2.2%, confirming the model accuracy in such circumstances.

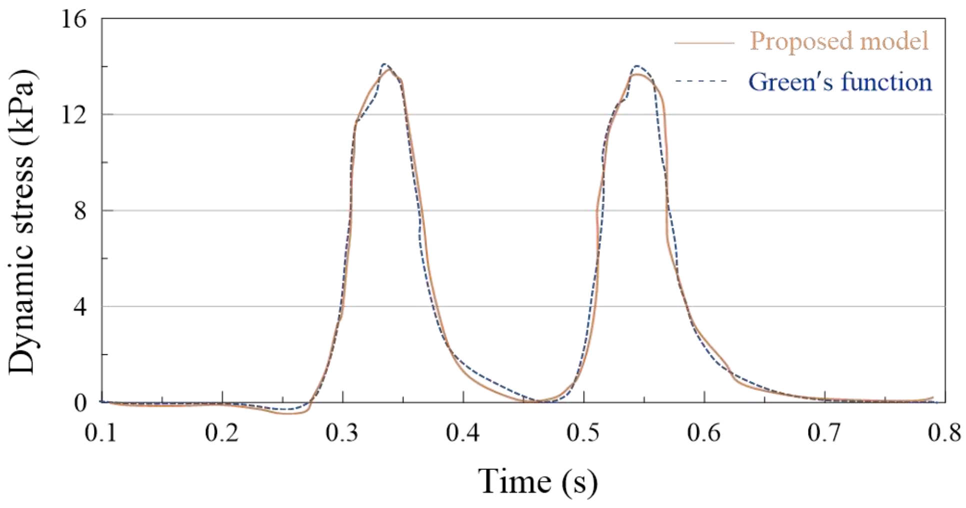

Figure 10. Comparison of dynamic stresses from the proposed model and Green's function

3.2 Validation 2: ASL field tests

After performing a numerical validation, a validation using field tests was performed. To do so measurement data was recorded on a test section of the Zhengzhou–Xuzhou railway line (CRTS III). ASL was experimentally applied and has been in operation since 2016. The slab track structure incorporates a 0.1 m thick

ASL overlying the upper roadbed [54]. Fig. 11 shows the photos taken from the test section. In the construction process, a monitoring system consisting of sensors, power supply systems, and a data acquisition unit were installed in the test section to monitor the dynamic performance of ASL during operation.

(a) (b)

Figure 11. Site photos of the instrumented rail line [66]: (a) asphaltic support layer; (b) integrated monitoring systems near the shoulder

Regarding numerical simulation, the track response due to the passage of a CRH380 train was considered, running at 350 km/h, and with an axle load of 170 kN (Appendix A). The primary parameters for the CRTS III track system are the same as in Table 1 with track irregularity.

Asphalt concrete is a viscoelastic material whose dynamic behaviour is influenced by temperature and loading frequency [67,68]. Therefore, the asphalt concrete model is carefully described in this study, given its constitutive relation to the dynamic FE analysis. The viscoelasticity of asphalt concrete is characterized using the generalized Maxwell model in the form of the Prony series [69], whose coefficients were determined by extracting and testing in-situ samples:

1) Cores of asphalt concrete were drilled from test sections on the test railway line and subjected to dynamic modulus testing using universal testing apparatus;

2) The master curve of the dynamic modulus was fitted using the Williams–Landel–Ferry Equation [70] via the time–temperature superposition principle (Fig. 12);

3) The relaxation modulus was determined from the fitted master curves [71]. The least squares method

was then used to calculate the Prony series coefficients [69].

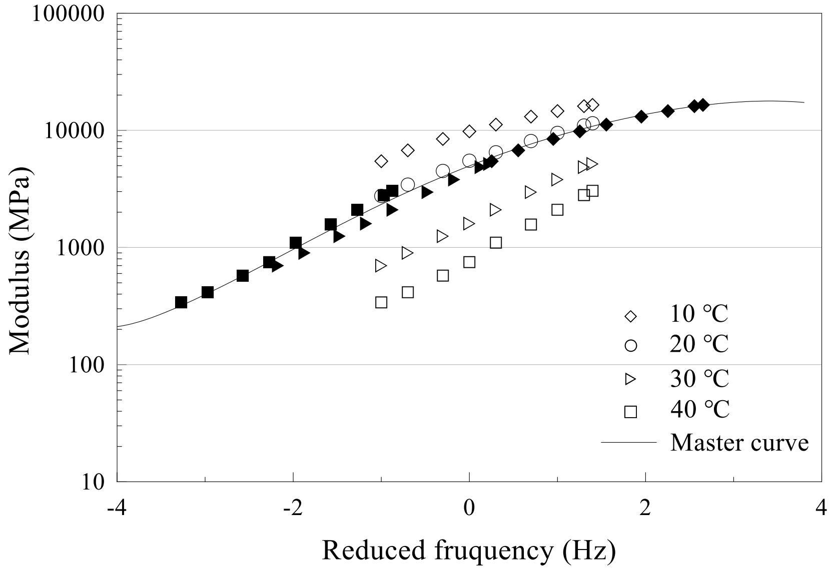

Figure 12. Master curve of asphalt concrete dynamic modulus [72]

Table 4 lists the coefficients of an eleventh-order Prony series for characterizing the constitutive relation of the asphalt concrete. These coefficients were directly imported into ABAQUS to simulate the dynamic behaviour of asphalt concrete. The fitting equation introduces a shift factor (a_T) to relate strains at different temperatures. The shift factor is calculated by:

$$\mathrm{Log}\, a_{\mathrm{T}} = \frac{-C_1(T - T_{\mathrm{ref}})}{C_2 + (T - T_{\mathrm{ref}})} \tag{6}$$

where log is the decadic logarithm, T_{ref} is the reference temperature, and C_1 and C_2 are positive constants dependent upon the T_{ref} and material properties.

Table 4. Prony series coefficients for the asphalt concrete ($T_{\mathrm{ref}} = 20$ °C) [72,73]

Serial number i	Relaxation time τ_i (s)	Prony series g_i	Serial number i	Relaxation time τ_i (s)	Prony series g_i
1	0.000 001	0.031 92	7	1	0.146 179
2	0.000 01	0.055 066	8	10	0.068 084
3	0.000 1	0.094 570	9	100	0.025 889
4	0.001	0.148 209	10	1,000	0.008 865
5	0.01	0.203 485	11	10,000	0.005 084
6	0.1	0.212 089			
C_1			11.7		
C_2			91.2		

Fig. 13 compares the field observations with simulation results of train-induced accelerations and displacements at the surface of the ASL.

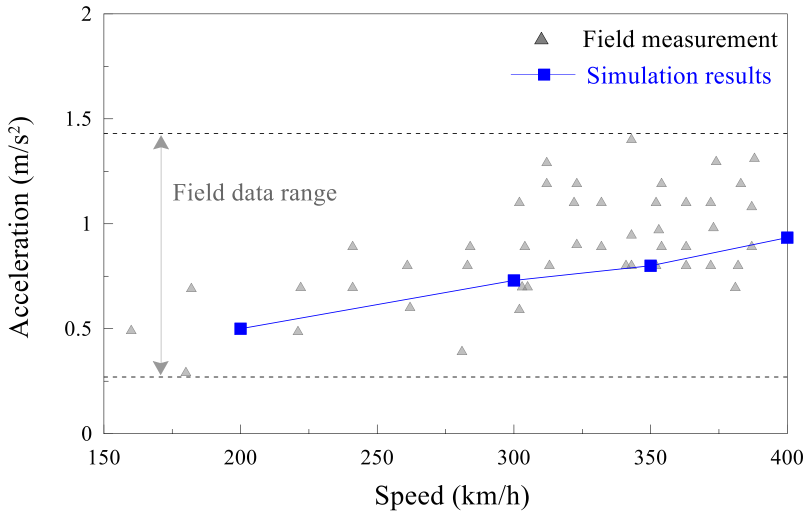

(a)

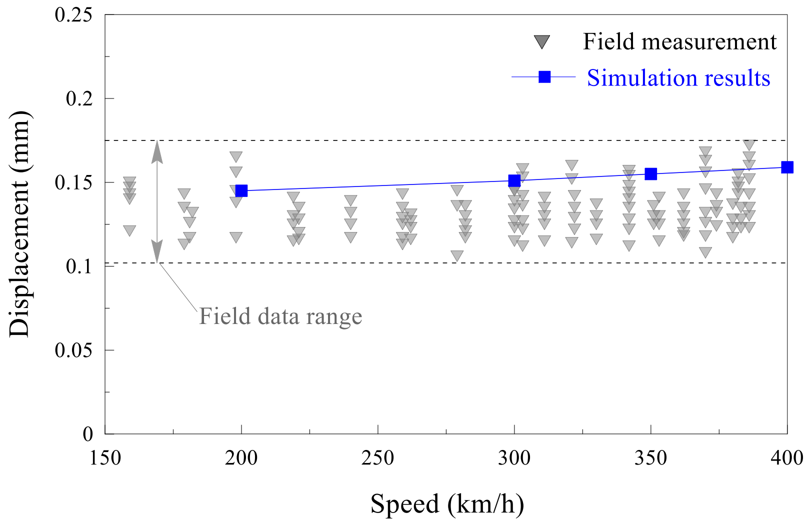

(b)

Figure 13. Field measurements and simulation results on top of ASL with varying operating speeds, (a) accelerations, and (b) displacements

A relatively linear best-fit relationship can be observed in Fig. 13 between the acceleration levels and the running speed. In contrast, the speed has limited influence on the displacement of the upper ASL surface. Across the speed levels, the measured displacements are scattered, ranging from 0.10 mm to 0.17 mm; while the variations in simulated values with operating speed are less significant, ranging from 0.115 mm to 0.125 mm. The simulated values always fall within the range of in-situ measurements, suggesting that the simulation is consistent with field observations. Considering the simulation models' performances in the two scenarios, it is possible to conclude that the two-step modelling framework is practical for studying the dynamic responses of ASL in slab track systems.

4. Results and analysis

Based on the validated two-step modelling approach, the dynamic behaviour of ASL's under moving train loads is simulated and assessed to reveal the material's role in the vibration and mechanical responses of slab track systems. Three representative positions (A, B, and C) are selected to evaluate the longitudinal structural discontinuities of slab tracks, as shown in Fig. 14. Considering a CRH380 vehicle running on the CRTS III slab track system, the model is developed with different ASL thicknesses: 0, 0.05, 0.07, 0.10, and 0.15 m. The ambient temperature is set to 20 °C, and a train speed of 400 km/h and axle load of 170 kN are considered for all models. To understand ASL behaviour, dynamic stresses and displacements are considered because they are critical design indexes for the subgrade. Accelerations are studied because they are related to ride comfort, while tensile and vertical strains are studied due to their relationship with asphalt concrete durability.

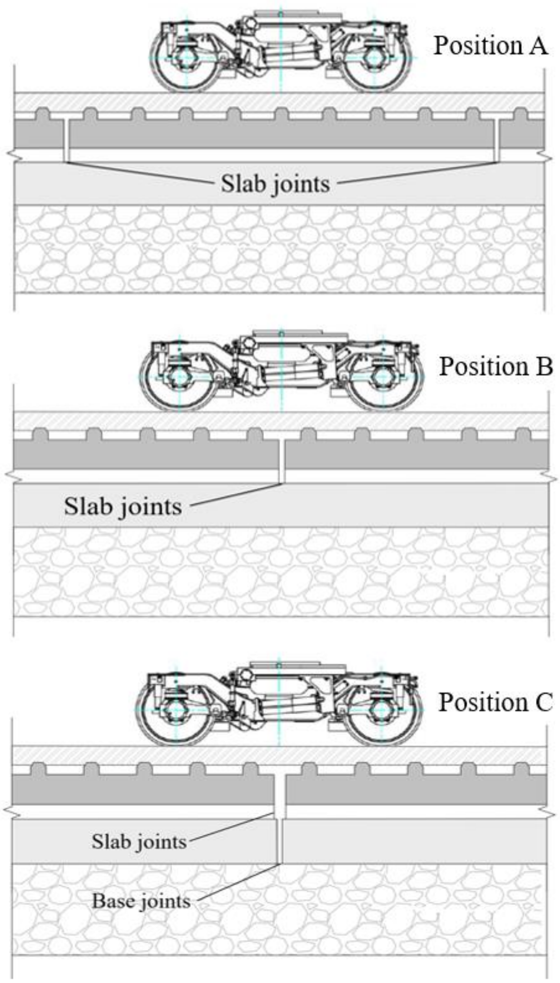

Figure 14. Three representative slab joint positions

4.1 Dynamic stresses

The ASL and base models exhibit a similar transverse stress distribution pattern, regardless whether the double-axle load is imposed on continuous (position A) or discontinuous (position B and position C) locations. From the symmetrical axis of structures to the slab edge, the train-induced stress is uniformly distributed in the transverse direction, consistent with field observations and previous findings [74,75], while a stress concentration occurs at the edges of concrete base. According to the approach in Ref. [76], the mean stress in each section can be calculated by the effective area and stress distribution on it. Taking a 0.05 m thick ASL as an example, Fig. 15 shows the dynamic stress histories at points A, B, and C on the ASL surface, while the stresses on the AUR surface are displayed in Fig. 16. Due to their similar pattern, only the average dynamics stress across the three lateral locations are shown in Fig. 16.

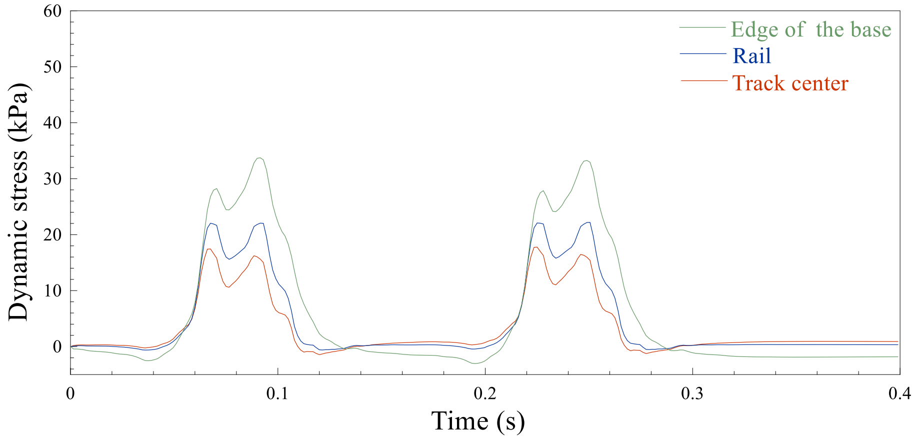
Edge of the base
Rail
Track center
Dynamic stress (kPa)
Time (s)
60
50
40
30
20
10
0
0
0.1
0.2
0.3
0.4

(a)

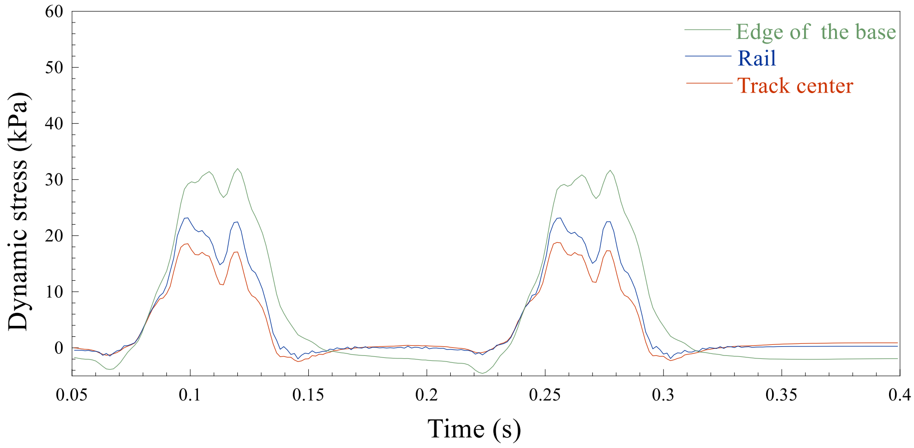
Edge of the base
Rail
Track center
Dynamic stress (kPa)
Time (s)
60
50
40
30
20
10
0
0.05
0.1
0.15
0.2
0.25
0.3
0.35
0.4

(b)

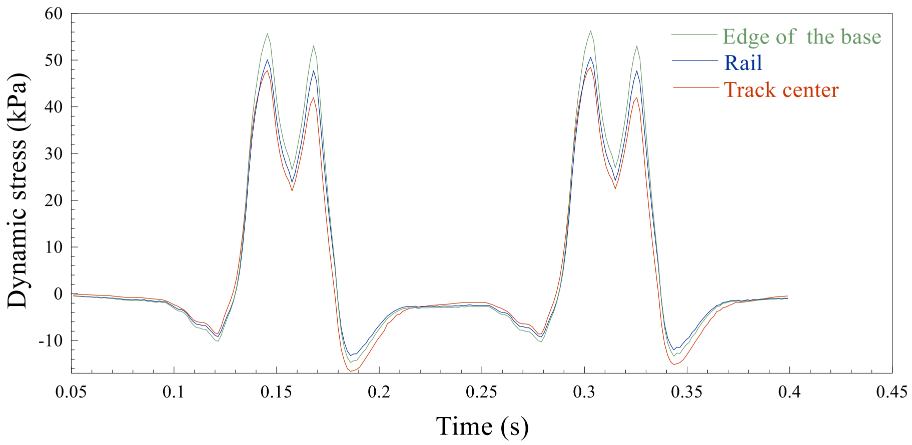
Edge of the base
Rail
Track center
Dynamic stress (kPa)
Time (s)
60
50
40
30
20
10
0
-10
0.05
0.1
0.15
0.2
0.25
0.3
0.35
0.4
0.45

(c)

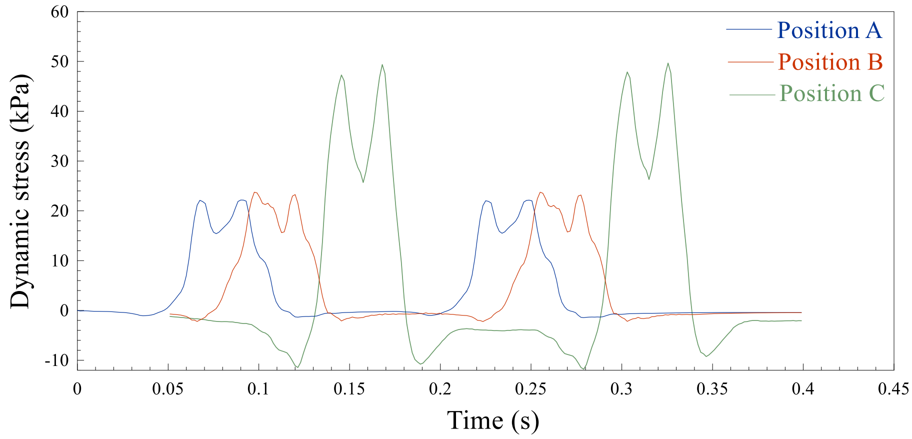

(d)

Figure 15. Stress time histories on the upper surface of ASL: (a) position A; (b) position B; (c) position C; (d) averaged dynamic stress across three lateral locations (ASL thickness = 0.05 m)

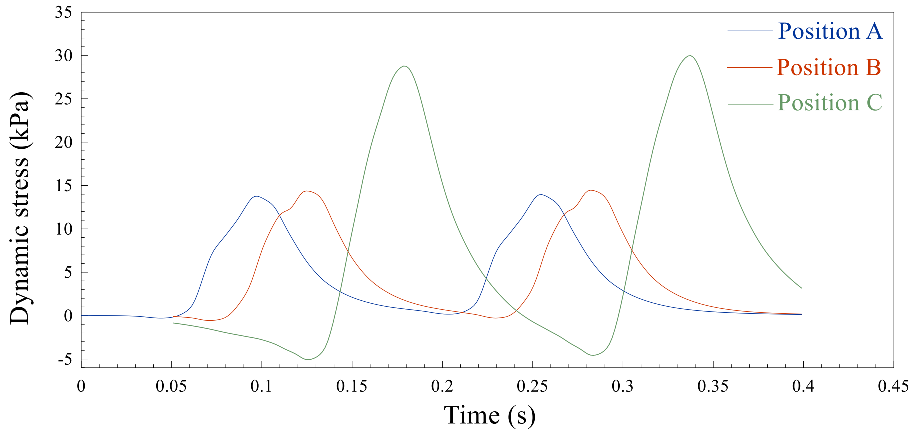

Figure 16. Stress time histories on the surface of the upper roadbed (ASL thickness = 0.05 m)

Comparing the stress response at the ASL and AUR surfaces, the variations in stress levels across different loading points have a similar pattern. The induced stress peaks are largest at point C, followed by points B and A. Note that the stress difference between points A and B is minimal, while the stress peaks at point C are substantially higher than at the other locations. The presence of expansion joints reduces the track structure stiffness, resulting in a stress concentration below the longitudinal discontinuities. The expansion joints between adjacent concrete bases contribute more to the surface stress than those between track slabs.

The calculated stress peaks on ASL, AUR and ALR, accounting for the layer thickness and loading positions, are listed in Table 5.

Table 5. Dynamic stress peaks on the surface of ASL, AUR, and ALR

Thickness of ASL (m)	Stress on surface of ASL (kPa)			Stress on surface of AUR (kPa)			Stress on surface of ALR (kPa)		
	Position A	Position B	Position C	Position A	Position B	Position C	Position A	Position B	Position C
0	/	/	/	16.14	17.05	33.40	13.90	14.01	18.42
0.05	22.17	23.75	49.67	13.94	14.48	28.48	13.30	13.36	17.36
0.07	24.25	25.66	54.91	13.82	14.29	26.63	13.09	13.12	17.14
0.10	28.62	29.02	63.86	13.52	13.89	23.98	12.77	12.76	16.79
0.15	30.74	33.98	70.12	12.51	12.70	21.98	12.15	12.11	15.92

Increasing the thickness of ASL decreases the corresponding stress peak on the surface of AUR and ALR. While the peak stress levels on the surface of the subgrade with ASL are higher than those of the base model (no ASL), the peak stress levels increase with the increasing thickness of ASL. As the modulus of asphalt concrete is higher than that of graded gravel, the stiffness of the ASL is greater than that of upper roadbed, leading to higher stress on the surface of the subgrade. In the same way, the bending stiffness of ASL increases with increasing ASL thickness, leading to higher stress levels.

4.2 Deflections of roadbed surface

Fig. 17 shows the dynamic displacement time histories on top of a 0.05 m thick ASL at the three different monitoring positions. The minimum displacement occurs at position A, slightly lower than the peak at position B. In contrast, the maximum displacement occurs at position C, which is significantly higher than the former two. The displacement patterns are comparable to those observed for the dynamic stress time histories across different positions.

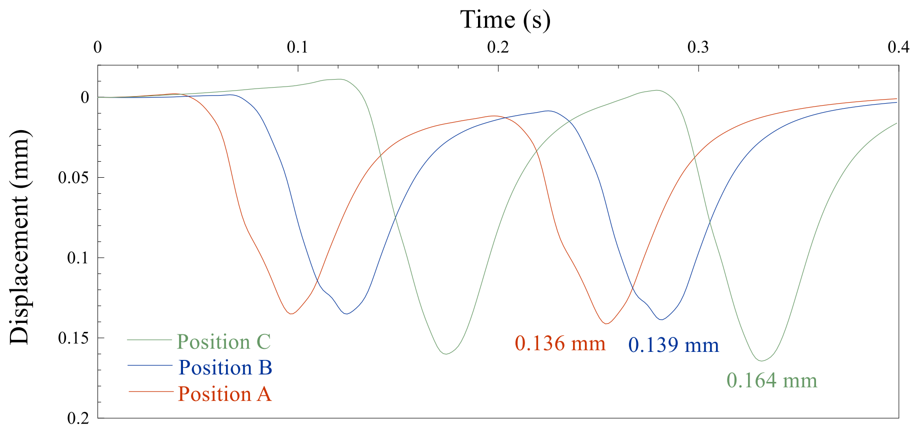

Figure 17. Deformation time histories of three longitudinal positions (ASL thickness = 0.05 m)

The peak dynamic displacement on the ASL surface against the ASL thickness is provided in Table 6.

Table 6. Dynamic displacement on the surface of ASL

Thickness of ASL (m)	Displacement on surface of ASL (mm)		
	Position A	Position B	Position C
0	0.139	0.142	0.173
0.05	0.136	0.139	0.164
0.07	0.134	0.136	0.162
0.10	0.132	0.133	0.159
0.15	0.124	0.125	0.149

The displacement peak occurs at position C for a specific ASL thickness, and an insignificant difference is observed between positions A and B. Under longitudinal discontinuities, the calculated maximum displacements satisfy the specification requirements (0. 22 m in slab tracks) suggested in [16]. As the thickness of ASL increases, all displacement peaks across different longitudinal locations decrease.

4.3 Accelerations

Fig. 18 plots the acceleration time histories on the surface of the 0.05 m thick ASL and AUR, in which the acceleration responses are compared between three positions. At each specific longitudinal location, the acceleration responses (magnitude and phase) on the two structural layers of the asphaltic track system are similar. Considering the different locations, the maximum acceleration magnitude occurs at position A, followed by positions B and C. The maximum acceleration amplitude is observed in the continuous part of the structure (position A).

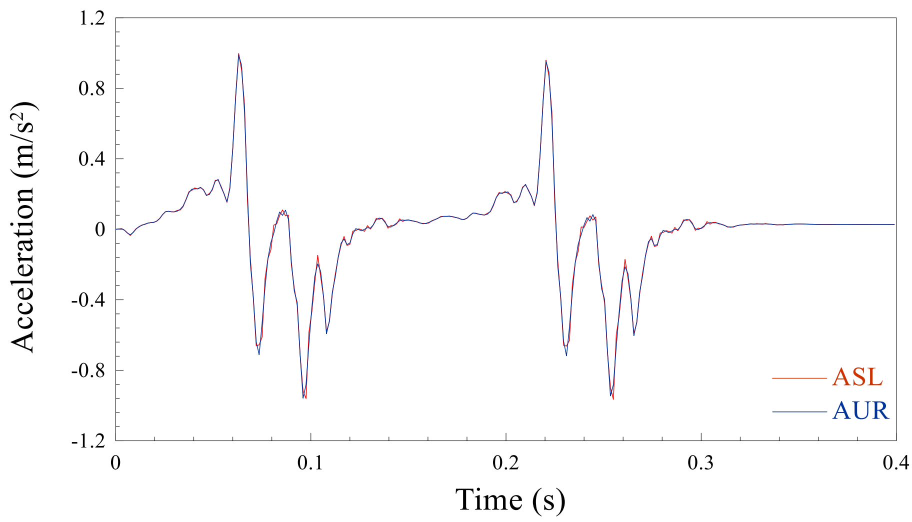

(a)

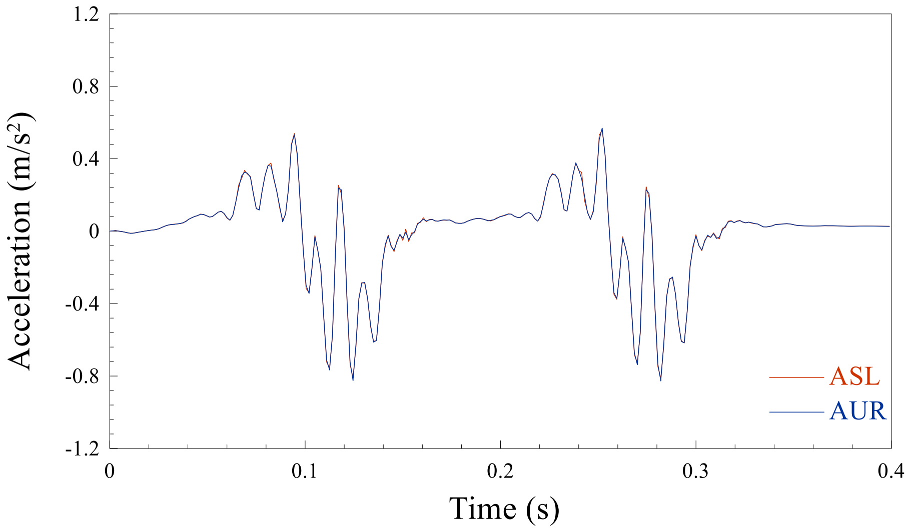

(b)

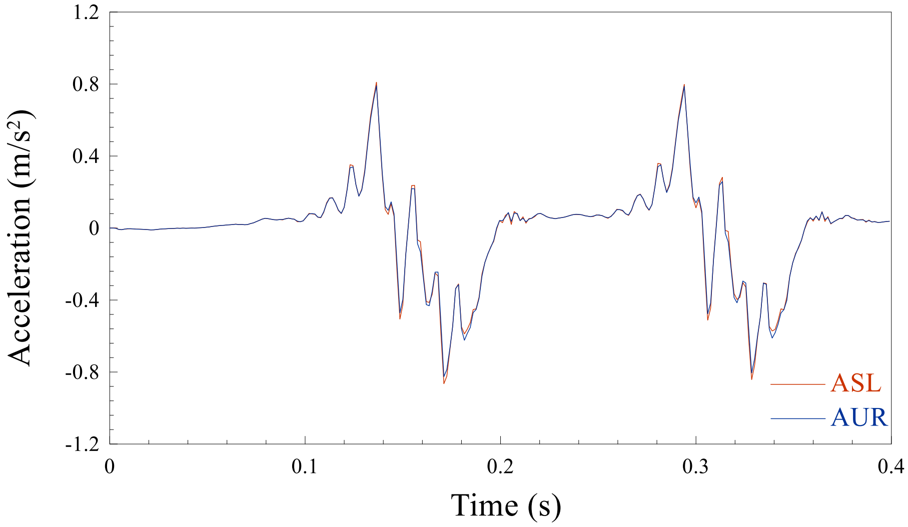

(c)

Figure 18. Acceleration time histories of ASL and AUR underneath three longitudinal positions: (a) position A, (b) position B, (c) position C (ASL thickness = 0.05 m)

The relationship between vertical acceleration amplitudes and ASL thickness are presented in Table 7, considering the longitudinal positions and base model. In asphaltic track systems, the trends at three positions are similar and manifest as acceleration amplitude decreasing with increasing ASL thickness. The introduction of ASL decreases the acceleration amplitude on the roadbed surface compared to the base model, which demonstrates the vibration damping effect of the reinforced track structure.

Table 7. Acceleration on the surface of ASL

Thickness of ASL (m)	Acceleration on surface of ASL (m/s^2)

	Position A	Position B	Position C
0	1.025	0.882	0.816
0.05	0.960	0.840	0.729
0.07	0.955	0.833	0.723
0.10	0.938	0.818	0.702
0.15	0.895	0.785	0.644

4.4 Tensile and vertical strains within ASL

The longitudinal and transverse tensile strains at the bottom of the 0.05 m thick ASL are displayed in Fig. 19. The lateral tensile strain remains positive during the loading–unloading phase, indicating that the asphalt concrete is constantly subjected to tensile loads in the lateral direction as one vehicle travels through. During the passage of the double-axle load, the longitudinal tensile strain varies from a negative value to a positive value. Unlike the lateral response, the bottom of asphalt concrete experiences compression and tension; each strain peak identified from the time history curves corresponds to the centre of one bogie (x-axis: time domain to the spatial location).

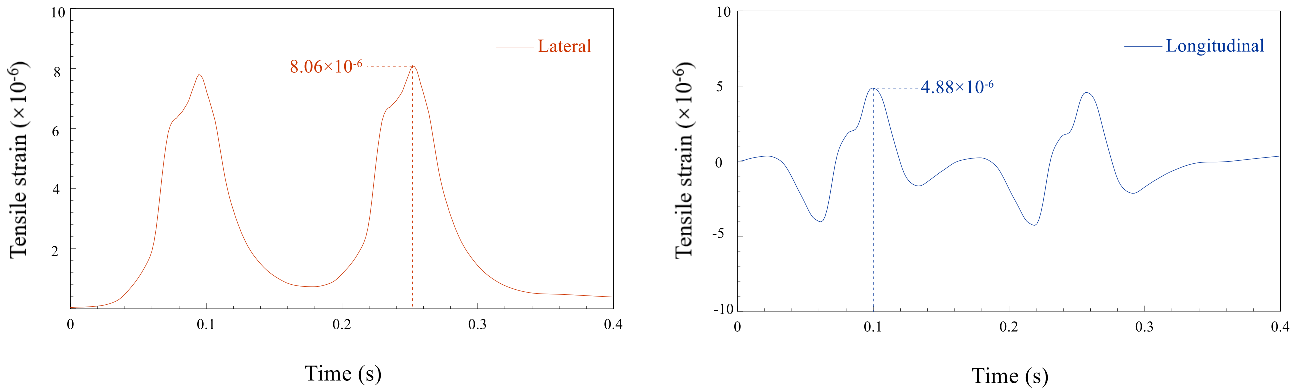

(a)

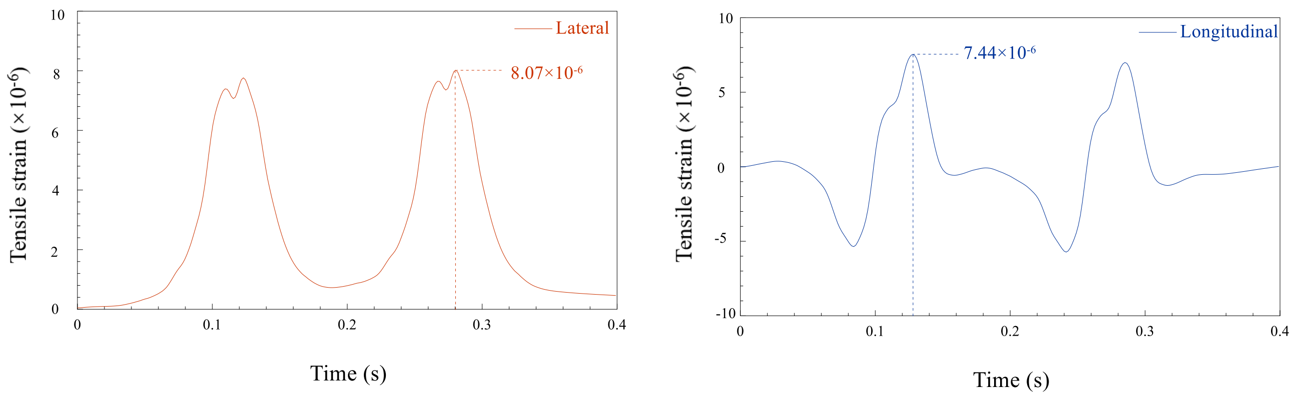

(b)

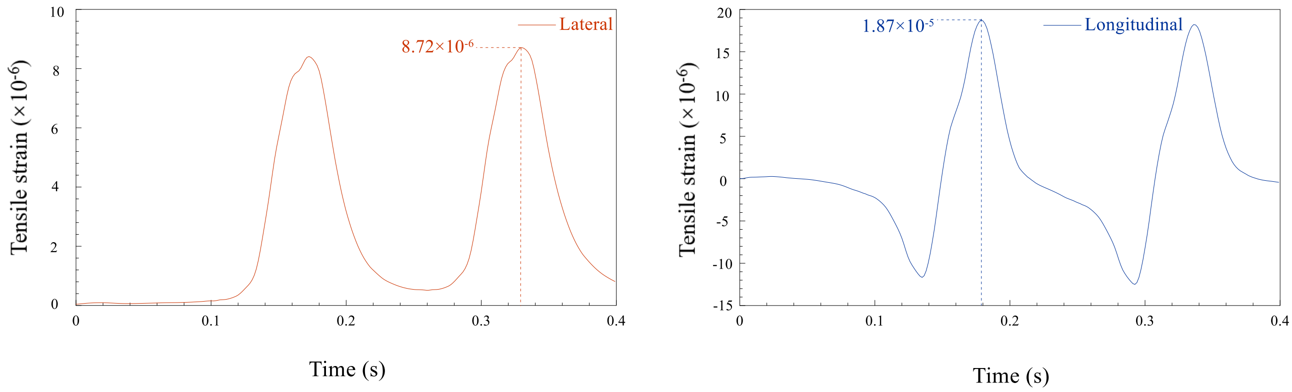

(c)

Figure 19. Lateral and longitudinal tensile strain at the bottom of ASL: (a) position A, (b) position B, (c) position C (ASL thickness = 0.05 m)

Table 8 demonstrates the variation in lateral and longitudinal tensile strains with ASL thickness, in which the strain responses between the three locations are compared. Under the same thickness, lateral and longitudinal tensile strains are at a minimum at position A, while they are at a maximum at position C. The expansion joints located between the concrete bases result in a marked increase in the tensile strains at the ASL base. At position C, the longitudinal tensile strain is significantly higher than the lateral tensile strain. When assessing the impact of layer thickness on the strain response, one observes that the tensile strain decreases with increasing ASL thickness in the lateral direction. At the same time, it increases with an increasing layer thickness in the longitudinal direction. The thickness effect is more significant on the strain response at position C than at positions A and B. Since the longitudinal tensile strain is critical to ASL fatigue life (serviceability), increasing the ASL thickness is not conducive to asphalt durability.

Table 8. Tensile strains on the surface on the bottom of ASL

Thickness of ASL (m)	Lateral tensile strains on surface of ASL			Longitudinal tensile strains on surface of ASL		
	Position A	Position B	Position C	Position A	Position B	Position C
0.05	8.06×10^{-6}	8.07×10^{-6}	8.72×10^{-6}	4.88×10^{-6}	7.44×10^{-6}	1.87×10^{-5}
0.07	7.81×10^{-6}	7.82×10^{-6}	8.43×10^{-6}	5.11×10^{-6}	7.57×10^{-6}	2.14×10^{-5}
0.10	7.49×10^{-6}	7.52×10^{-6}	8.2×10^{-6}	5.38×10^{-6}	7.64×10^{-6}	2.32×10^{-5}
0.15	7.02×10^{-6}	7.06×10^{-6}	7.83×10^{-6}	6.11×10^{-6}	7.76×10^{-6}	2.57×10^{-5}

For an ASL thickness of 0.05 m, Fig. 20 shows the time histories of vertical strains on top of AUR and ALR, in which the responses between the three positions are compared. Table 9 compares the vertical strain on top of AUR and ALR under various ASL thicknesses. The maximum vertical strain occurs at position C. On top of AUR and ALR, the vertical strains decrease with thicker ASL, suggesting that the use of ASL reduces the strain levels in the roadbeds, especially in the upper layer.

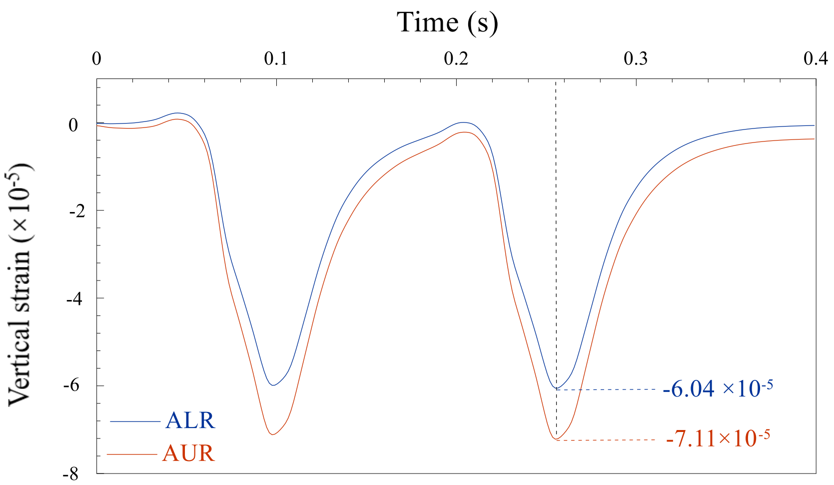

(a)

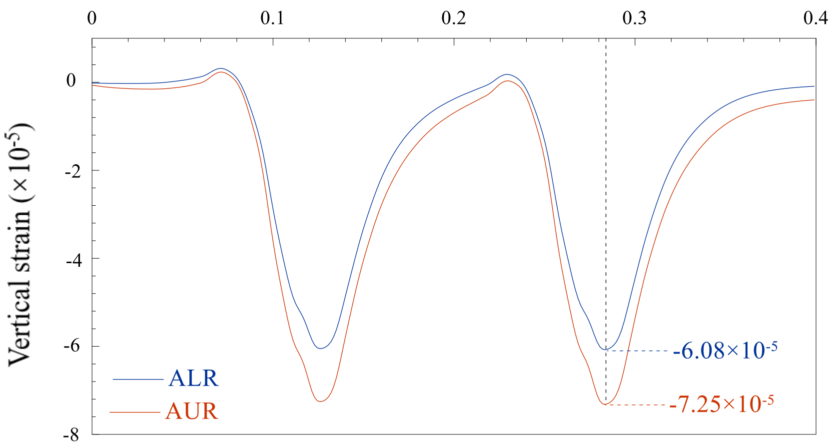

(b)

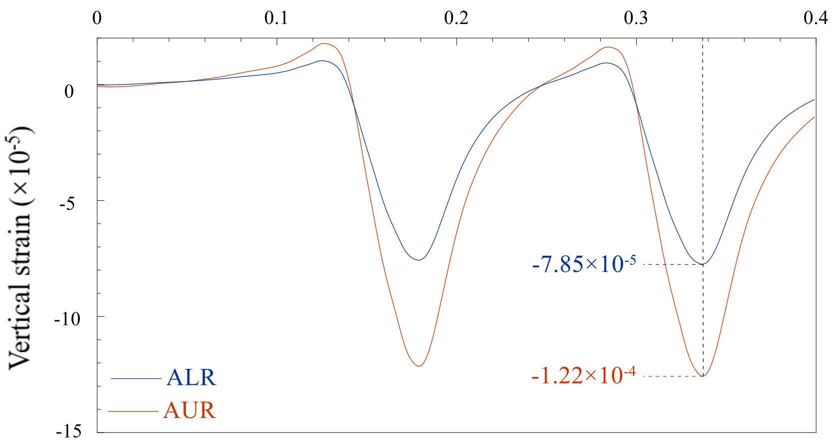

(c)

Figure 20. Vertical strain on the surface of the upper and lower roadbeds: (a) position A, (b) position B, (c) position C (ASL thickness = 0.05 m)

Table 9. Vertical strains on the surface of AUR and ALR

Thickness of ASL (m)	Vertical strains on surface of AUR			Vertical strains on surface of ALR		
	Position A	Position B	Position C	Position A	Position B	Position C
0	-9.38×10^{-5}	-9.66×10^{-5}	-1.72×10^{-4}	-6.20×10^{-5}	-6.24×10^{-5}	-7.95×10^{-5}
0.05	-7.11×10^{-5}	-7.25×10^{-5}	-1.22×10^{-4}	-6.04×10^{-5}	-6.08×10^{-5}	-7.85×10^{-5}
0.07	-6.63×10^{-5}	-6.75×10^{-5}	$-1.12\text{E}\times10^{-4}$	-6.02×10^{-5}	-6.05×10^{-5}	-7.84×10^{-5}
0.10	-6.09×10^{-5}	-6.17×10^{-5}	-9.86×10^{-5}	-5.93×10^{-5}	-5.93×10^{-5}	-7.74×10^{-5}
0.15	-5.43×10^{-5}	-5.48×10^{-5}	-9.14×10^{-5}	-5.55×10^{-5}	-5.57×10^{-5}	-7.26×10^{-5}

5. Design considerations for ASL

5.1 Asphalt concrete durability

According to the design method proposed by the Asphalt Institute [77], the horizontal tensile strain (ε_r) at the base of the ASL and the compressional strain (ε_z) on the surface of the gravel roadbed (AUR) are indicators for evaluating the asphalt's fatigue cracking potential and the capacity to resist permanent deformation.

Although both indicators are commonly used in asphalt pavement design, the stress paths induced under moving train loads differ from highway environments. For example, considering highway structures, the asphalt pavement carries the tire load directly, while for railways the train load is distributed through the rails, sleeper, and track superstructure before reaching the ASL surface. Therefore, the multilayered elastic theory commonly used in pavement design does not apply for calculating the tensile strains at the surface of the ASL, or the compressional strains at the surface of the railway AUR. To overcome this, this study obtains the strain level of ASL under moving train loads through FE track-ground modelling, based on which fatigue cracking and permanent deformation are checked. It should be noted that asphalt trackbed mix design is typically similar to that for highway asphalt pavements. Therefore although the strain parameters of ASL are calculated by the FE method, a highway pavement approach is used for evaluating the durability of ASL.

The primary goal of examining asphalt fatigue is to ensure the number of loadings during its service life doesn't exceeded the allowable number of loadings concerning fatigue damage, which is governed by the tensile strain at the base of ASL. An empirical formula is proposed [77] for the fatigue testing of asphalt concrete:

$$N_a = 18.4 \times C \times 6.167 \times 10^{-5} {\varepsilon_r}^{-3.291} {E_A}^{-0.854} \tag{8}$$

where N_a is the number of load applications required by fatigue damage; ε_r is the maximum tensile strain at the base of ASL; E_A is the elastic modulus of asphalt concrete (MPa); and C is a constant related to the voids filled with asphalt (VFA), determined by:

$$C = 10^{4.84(\mathrm{VFA}-0.6875)} \tag{9}$$

The value of VFA can be prescribed using the Marshall mix design method: 65% - 75% for heavy traffic (equivalent number of standard axles > 10^6), 65% - 78% for medium traffic (equivalent number of standard axles between 10^4 and 10^6), and 70% - 80% for light traffic (equivalent number of standard axles < 10^4).

Local deformation governs the structural deformation of ASL, meaning vertical strains should be controlled within a permissible range to prevent cracks developing. According to the experimental data provided by the American Association of State Highway Officials (AASHO), the number of loadings concerning allowable permanent deformation (N_s) is calculated by:

$$N_s = 1.365 \times 10^{-9} {\varepsilon_z}^{-4.477} \tag{10}$$

where ε_z is the compressional strain on top of AUR. ASL of rail infrastructure is underlain by AUR, comparable to the base and subbase layers of a road pavement structure. Note that because the surface layer of an asphalt pavement carries vehicle loads directly, the strength of base and subbase materials is generally higher than that of AUR and ALR. To control the permanent deformation of ASL, it is recommended that two indicators are used: the compressional strain on the AUR surface (ε_{zu}) and the compression strain on the ALR surface (ε_{zl}).

The elastic modulus of asphalt concrete is influenced by ambient temperature, meaning the degree of fatigue damage can be estimated by summing it over a desired number of seasons. As an illustration, the ambient temperature is assumed as 20 °C for spring and autumn, 5 °C for winter, and 40 °C for summer to set the thermal conditions in FE submodels. To satisfy the durability requirements, the cumulative degree of fatigue damage and degree of deformation-induced damage over the design service life should be less than 1.0. The values of m_a and m_s are obtained by:

$$m_a = \sum_{i=1}^{4} m_{ai} = \sum_{i=1}^{4} \frac{N_i}{N_{ai}} \tag{11a}$$

$$m_s = \sum_{i=1}^{4} m_{si} = \sum_{i=1}^{4} \frac{N_i}{N_{si}} \tag{11b}$$

where m_a and m_{ai} are the degrees of fatigue damage per year and season respectively; m_s and m_{si} are the degree of deformation-induced damage per year and season respectively; subscript i = 1, 2, 3, and 4, corresponding to four seasons in one year; N_i is the number of bogie passages in each season; and N_{ai} and N_{si} are the allowable numbers of bogie passages defined for each season, related to the fatigue and deformation-induced damage respectively. N_{ai} and N_{si} are fixed values if the design service life has been determined. The calculated durability indexes of asphalt material for different ASL thicknesses (0.05, 0.07, 0.10, 0.15 m) are provided in Appendix B.

Assuming a 100-year service life for slab tracks and an annual loading of 1 million cycles, the cumulative fatigue and deformation-induced damage for all ASL thicknesses is less than 1.0. This indicates that the long-term durability of ASL satisfies serviceability requirements. For the increased thicknesses, the stresses on the AUR and ALR surfaces decrease, which is beneficial to the deformation-related durability (cumulative degree decreases from 0.319 to 0.123). Alternatively, the tensile strain at the base of the ASL increases with increasing thickness, resulting in elevated fatigue risk (cumulative degree increases from 0.196 to 0.622).

5.2 Roadbed design

It's good practice that cumulative plastic deformation should not develop in the slab track roadbeds of railway lines [78], and the strains should not exceed the threshold defined in specifications [16]. In the case of upper and lower roadbeds, the relationship between the elastic threshold ([ε]) for coarse fills and the K_{30} (MPa/m) value can be expressed as [65]:

$$[\varepsilon] = 0.28K_{30} + 107 \tag{12}$$

where K_{30} is modulus of subgrade reaction (MPa/m); ε is strain for coarse fills (10^{-6}); [ε] means the elastic threshold (10^{-6}) for coarse fills corresponds to a certain value of K_{30}. According to the K_{30} plate load test, the elastic modulus of coarse fills can be obtained by [78,79]:

$$E = 0.225 K_{30} \beta \tag{13}$$

where β is the correction factor (m), which can be determined using established approaches [78,79]. Given a specific value of K_{30}, the threshold strain and stress can be calculated for coarse fills, and the results are summarized in Table 10.

Table 10. Threshold stress of coarse fills in roadbeds varying with K_{30} values

K_{30} (MPa/m)	Elastic modulus (MPa)	Threshold strain ($\times 10^{-6}$)	Threshold stress (kPa)
190	228.72	160.2	36.64
180	218.23	157.4	34.35
170	207.59	154.6	32.09
160	196.80	151.8	29.87
150	185.85	149	27.69
140	174.73	146.2	25.55
130	163.46	143.4	23.44
120	152.01	140.6	21.37
110	140.39	137.8	19.35
100	128.60	135	17.36
90	116.62	132.2	15.42

Based on the simulation results of AUR and ALR, the worst-case scenario of additional stress at different positions is likely to be directly below the expansion joints between adjacent concrete bases (position C). Combining the relationship between threshold stress and K_{30} (Table 10) with the ASL thickness–stress relation (Table 5, position C), it is possible to back-calculate the threshold [K_{30}], with varying ASL thickness, as shown in Fig. 21 (linear interpolation is used between discrete data points).

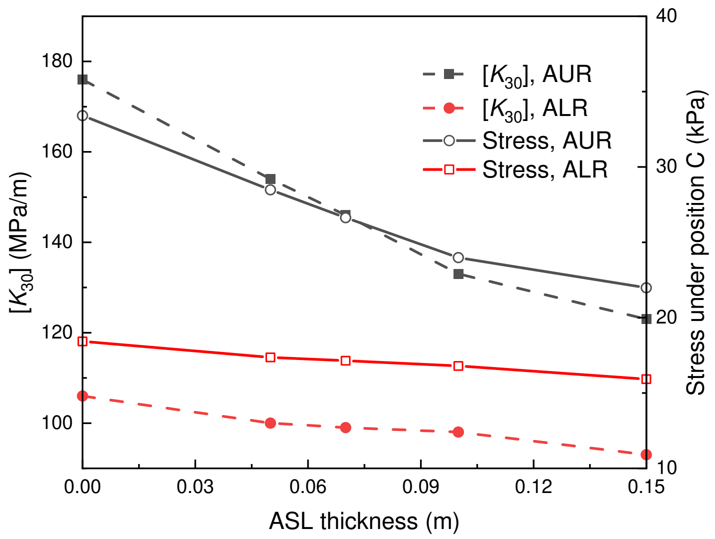

Figure 21. Effect of ASL thickness on stress level and back-calculated [K_{30}] of AUR and ALR.

Fig. 21 indicates that increasing the ASL thickness leads to a decrease in the design value of K_{30} for AUR and ALR, and the decrease is more prominent for AUR. In conventional slab tracks, [K_{30}] is approximately 176 MPa/m in the upper roadbed and 106 MPa/m in the lower roadbed. As per [16], the design K_{30} value should be larger than 190 MPa/m in upper roadbed and 130−150 MPa in LR. If we consider a reduction factor of 0.75 for fills under immersed conditions (worst-case scenario), the actual K_{30} may decrease to 142.5 MPa < 176 MPa/m in upper roadbed [80]. The trial calculations in Fig. 21 reveal that a minimum ASL thickness of 0.07 m is necessary for preventing cumulative plastic deformation in the AUR if immersed conditions are involved. In addition, asphalt concrete construction techniques typically require the paving thickness of single layers to be less than 0.1 m. If the ASL thickness exceeds 0.1 m, double-layer paving technology is usually used, resulting in a substantial increase in construction costs [72]. Therefore the optimum ASL thickness is likely to lie within 0.07–0.10 m for slab tracks.

6. Conclusions

The application of ASL for slab track systems was studied using a two-step modelling approach validated using analytical outcomes and field measurements. To investigate slab track dynamics with ASL, track system models with different ASL thicknesses were developed and a conventional slab track was used as a base model. The stresses, deflections, accelerations and strains within both continuous and discontinuous track structures were analysed. Then the durability of asphalt concrete under seasonal temperature variations was examined and the optimal design thickness for ASL discussed.

It was found that the application of ASL within slab track systems can improve the mechanical performance of the supporting foundation. Increasing asphaltic thickness decreases the corresponding stress, deflection, acceleration, and strain peaks on the surface of the AUR and ALR. While the dynamic stresses on the surface of ASL and longitudinal tensile strain at the bottom of ASL increase with the increasing ASL thickness, which is not conductive to the mechanical performance of ASL itself. The reduced track bending stiffness at expansion joints causes stress concentrations below the longitudinal discontinuities, resulting in stress, deflection, and strain peaks significantly higher than that at locations positions further away from the joints.

ASLs meet the durability requirements for a 100-year service life considering the thickness range under test: 0.05–0.15 m. As the thickness increases, the maximum compressional strains in the upper and lower roadbeds decrease, while the longitudinal tensile strain at the base of the ASL increases. Considering plastic deformation and construction constraints, ASL thicknesses between 0.07 m and 0.10 m appear suitable for slab tracks. Further investigation of ASL assessments should incorporate the contribution of thermal regimes through coupled thermomechanical simulations and advanced asphalt concrete constitutive models.

Acknowledgements

The study was supported by the National Natural Science Foundation of China [Grant Nos. 41901073 and 52078435], the Royal Society (IEC\NSFC\211306 - International Exchanges 2021 Cost Share), and the 111 Project (B21011).

Declaration of Competing Interests

None.

Appendix A

The calculation parameters for the CRH2 vehicle are provided in Table A1.

Table A1. Calculation parameters for the CRH2 vehicle

Parameters	Symbols	Units	Values
Car body mass	M_c	kg	45,600
Car body pitch moment of inertia	J_c	$kg{\cdot}m^2$	2.231×10^6
Bogie mass	M_t	kg	3,200
Bogie pitch moment of inertia	J_t	$kg{\cdot}m^2$	1,752
Wheelset mass	M_w	kg	2,000
Primary suspension stiffness	K_{pz}	$N{\cdot}m^{-1}$	2.352×10^6
Primary suspension damping	C_{pz}	$N{\cdot}s{\cdot}m^{-1}$	3.92×10^4
Secondary suspension stiffness	K_{sz}	$N{\cdot}m^{-1}$	1.982×10^6
Secondary suspension damping	C_{sz}	$N{\cdot}s{\cdot}m^{-1}$	1.96×10^4
Bogie spacing	L_c	m	17.5
Wheel distance	L_t	m	2.5
Wheel rolling radius	R_w	m	0.43

The calculation parameters for the CRH380 vehicle are provided in Table A2.

Table A2. Calculation parameters for the CRH380 vehicle

Parameters	Symbols	Units	Values
Car body mass + dwt	M_c	kg	34,934+8,000
Car body pitch moment of inertia	J_c	$kg{\cdot}m^2$	1.7118×10^6
Bogie mass	M_t	kg	3,300
Bogie pitch moment of inertia	J_t	$kg{\cdot}m^2$	1,807
Wheelset mass	M_w	kg	1,780
Primary suspension stiffness	K_{pz}	$N{\cdot}m^{-1}$	1.176×10^5
Primary suspension damping	C_{pz}	$N{\cdot}s{\cdot}m^{-1}$	1.0×10^4
Secondary suspension stiffness	K_{sz}	$N{\cdot}m^{-1}$	2.4×10^5
Secondary suspension damping	C_{sz}	$N{\cdot}s{\cdot}m^{-1}$	2.0×10^4
Bogie spacing	L_c	m	17.5
Wheel distance	L_t	m	2.5
Design axle load	P_0	kN	170
Vehicle length	L_v	m	25
Wheel rolling radius	R_w	m	0.43

Appendix B

The calculation results of the durability check for asphalt material under four ASL thicknesses are provided in Tables B1, B2, B3, and B4, where four seasons are differentiated. ε_{r1} and ε_{r2} are the lateral and longitudinal tensile strain at the base of ASL, respectively; ε_r is the horizontal tensile strain, which equals max$\{\varepsilon_{r1}, \varepsilon_{r2}\}$; N_{ai} is the allowable number of bogie passages defined for each season related to fatigue damage; m_{ai} is the degree of fatigue damage per season; ε_{zu} and ε_{zl} are the compression strain on the AUR surface and on the ALR surface, respectively; ε_z is the maximum of ε_{zu} and ε_{zl}; N_{ai} is the allowable number of bogie passages defined for each season related to deformation-included damage; m_{ai} and m_{si} are the degree of fatigue deformation-induced damage per season, respectively; m_a and m_s are the degree of fatigue damage and deformation-induced damage per year, respectively.

Table B1. Essential parameters for durability with ASL thickness of 0.05 m

	Spring	Summer	Autumn	Winter
ε_{r1}	8.72×10^{-6}	1.33×10^{-5}	8.72×10^{-6}	8.40×10^{-6}
ε_{r2}	1.87×10^{-5}	1.91×10^{-5}	1.87×10^{-5}	1.85×10^{-5}
ε_r	1.87×10^{-5}	1.91×10^{-5}	1.87×10^{-5}	1.85×10^{-5}
N_{ai}	5.16×10^{8}	4.84×10^{8}	5.16×10^{8}	5.32×10^{8}
m_{ai}	4.85×10^{-4}	5.17×10^{-4}	4.85×10^{-4}	4.70×10^{-4}
ε_{zu}	1.22×10^{-4}	1.54×10^{-4}	1.22×10^{-4}	1.21×10^{-4}
ε_{zl}	7.85×10^{-5}	8.74×10^{-5}	7.85×10^{-5}	7.86×10^{-5}
ε_z	1.22×10^{-4}	1.54×10^{-4}	1.22×10^{-4}	1.21×10^{-4}
N_{si}	4.52×10^{8}	1.60×10^{8}	4.52×10^{8}	4.78×10^{8}
m_{si}	5.53×10^{-4}	1.56×10^{-3}	5.53×10^{-4}	5.23×10^{-4}
m_a	0.00196			
m_s	0.00319			

Table B2. Essential parameters for durability with ASL thickness of 0.07 m

	Spring	Summer	Autumn	Winter
ε_{r1}	8.43×10^{-6}	1.31×10^{-5}	8.43×10^{-6}	8.04×10^{-6}
ε_{r2}	2.14×10^{-5}	2.28×10^{-5}	2.14×10^{-5}	2.12×10^{-5}
ε_r	2.14×10^{-5}	2.28×10^{-5}	2.14×10^{-5}	2.12×10^{-5}
N_{ai}	3.32×10^{8}	2.69×10^{8}	3.32×10^{8}	3.45×10^{8}
m_{ai}	7.53×10^{-4}	9.30×10^{-4}	7.53×10^{-4}	7.25×10^{-4}
ε_{zu}	1.12×10^{-4}	1.46×10^{-4}	1.12×10^{-4}	1.11×10^{-4}
ε_{zl}	7.84×10^{-5}	8.36×10^{-5}	7.84×10^{-5}	7.81×10^{-5}
ε_z	1.12×10^{-4}	1.46×10^{-4}	1.12×10^{-4}	1.11×10^{-4}
N_{si}	6.53×10^{8}	2.01×10^{8}	6.53×10^{8}	6.92×10^{8}
m_{si}	3.83×10^{-4}	1.24×10^{-4}	3.83×10^{-4}	3.61×10^{-4}
m_a	0.00316			
m_s	0.00237			

Table B3. Essential parameters for durability with ASL thickness of 0.10 m

	Spring	Summer	Autumn	Winter
ε_{r1}	8.20×10^{-6}	1.24×10^{-5}	8.20×10^{-6}	7.73×10^{-6}
ε_{r2}	2.32×10^{-5}	2.82×10^{-5}	2.32×10^{-5}	2.28×10^{-5}
ε_{r}	2.32×10^{-5}	2.82×10^{-5}	2.32×10^{-5}	2.28×10^{-5}
N_{ai}	2.56×10^{8}	1.34×10^{8}	2.56×10^{8}	2.70×10^{8}
m_{ai}	9.77×10^{-4}	1.87×10^{-3}	9.77×10^{-4}	9.27×10^{-4}
ε_{zu}	9.86×10^{-5}	1.33×10^{-4}	9.86×10^{-5}	9.71×10^{-5}
ε_{zl}	7.74×10^{-5}	8.12×10^{-5}	7.74×10^{-5}	7.69×10^{-5}
ε_{z}	9.86×10^{-5}	1.33×10^{-4}	9.86×10^{-5}	9.71×10^{-5}
N_{si}	1.18×10^{9}	3.04×10^{8}	1.18×10^{9}	1.26×10^{9}
m_{si}	2.12×10^{-4}	8.22×10^{-4}	2.12×10^{-4}	1.99×10^{-4}
m_{a}	0.00475			
m_{s}	0.00145			

Table B4. Essential parameters for durability with ASL thickness of 0.15 m

	Spring	Summer	Autumn	Winter
ε_{r1}	7.827×10^{-6}	1.15×10^{-5}	7.827×10^{-6}	7.27×10^{-6}
ε_{r2}	2.57×10^{-5}	3.17×10^{-5}	2.57×10^{-5}	2.12×10^{-5}
ε_{r}	2.57×10^{-5}	3.17×10^{-5}	2.57×10^{-5}	2.12×10^{-5}
N_{ai}	1.81×10^{8}	9.14×10^{7}	1.81×10^{8}	3.43×10^{8}
m_{ai}	1.38×10^{-3}	2.73×10^{-3}	1.38×10^{-3}	7.30×10^{-4}
ε_{zu}	9.14×10^{-5}	1.32×10^{-4}	9.14×10^{-5}	8.96×10^{-5}
ε_{zl}	7.26×10^{-5}	7.92×10^{-5}	7.26×10^{-5}	7.15×10^{-5}
ε_{z}	9.14×10^{-5}	1.32×10^{-4}	9.14×10^{-5}	8.96×10^{-5}
N_{si}	1.65×10^{9}	3.19×10^{8}	1.65×10^{9}	1.81×10^{9}
m_{si}	1.51×10^{-4}	7.85×10^{-4}	1.51×10^{-4}	1.38×10^{-4}
m_{a}	0.00622			
m_{s}	0.00123			

References

[1] Lu C. A discussion on technologies for improving the operational speed of high-speed railway networks. Transp Saf Environ 2019;1:22–36.

[2] Ren J, Deng S, Zhang K, Wei D, Wu Q. Design theories and maintenance technologies of slab tracks for high-speed railways in China: a review. Transportation Safety and Environment 2021;3.

[3] Feng S-J, Zhang X-L, Wang L, Zheng Q-T, Du F-L, Wang Z-L. In situ experimental study on high speed train induced ground vibrations with the ballast-less track. Soil Dynamics and Earthquake Engineering 2017;102:195–214.

[4] Shan Y, Zhou S, Wang B, Ho CL. Differential Settlement Prediction of Ballasted Tracks in Bridge–Embankment Transition Zones. Journal of Geotechnical and Geoenvironmental Engineering 2020;146:04020075.

[5] Luo Q, Wu P, Wang T. Evaluating frost heave susceptibility of well-graded gravel for HSR subgrade based on orthogonal array testing. Transportation Geotechnics 2019;21:100283.

[6] Wang T, Ma H, Liu J, Luo Q, Wang Q, Zhan Y. Assessing frost heave susceptibility of gravelly soils based on multivariate adaptive regression splines model. Cold Regions Science and Technology 2021;181:103182.

[7] Wang T, Luo Q, Liu M, Wang L, Qi W. Physical modeling of train-induced mud pumping in substructure beneath ballastless slab track. Transportation Geotechnics 2020;23:100332.

[8] Liu C, Shan Y, Wang B, Zhou S, Wang C. Reinforcement load in geosynthetic-reinforced pile-supported model

embankments. Geotextiles and Geomembranes 2022;50:1135–46.
[9] Bian X, Wan Z, Zhao C, Cui Y, Chen Y. Mud pumping in the roadbed of ballastless high-speed railway. Géotechnique 2022:1–15.
[10] Lee S-H, Vo HV, Park D-W, Na I-H. Comparisons of structural behavior between level and cant area of asphalt concrete track. Construction and Building Materials 2017;153:578–87.
[11] Yang E, Wang KCP, Luo Q, Qiu Y. Asphalt Concrete Layer to Support Track Slab of High-Speed Railway. Transportation Research Record 2015;2505:6–14.
[12] Luo Q, Fu H, Liu K, Wang T, Feng G. Monitoring of train-induced responses at asphalt support layer of a high-speed ballasted track. Construction and Building Materials 2021;298:123909.
[13] Fang M, Hu T, Rose JG. Geometric composition, structural behavior and material design for asphalt trackbed: A review. Construction and Building Materials 2020;262:120755.
[14] Xiao X, Cai D, Lou L, Shi Y, Xiao F. Application of asphalt based materials in railway systems: A review. Construction and Building Materials 2021;304:124630.
[15] Yu Z, Connolly DP, Woodward PK, Laghrouche O. Settlement behaviour of hybrid asphalt-ballast railway tracks. Construction and Building Materials 2019;208:808–17.
[16] TB10621-2014. Code for Design of High-Speed Railway, The National Railway Administration of China: 2014.
[17] Jadidi K, Esmaeili M, Kalantari M, Khalili M, Karakouzian M. A Review of Different Aspects of Applying Asphalt and Bituminous Mixes under a Railway Track. Materials (Basel) 2020;14:169.
[18] Sharma DK, Swami BL, Vyas AK. Performance evaluation of hot mix asphalt containing copper slag. Materials Today: Proceedings 2021;38:1241–4.
[19] Teixeira PF, López-Pita A. Viability of using a bituminous sub-ballast layer on high-speed ballasted tracks. Proceedings of the International Conferences on the Bearing Capacity of Roads, Railways and Airfields 2005.
[20] J.G. Rose, H.M. Lees. Long-Term Assessment of Asphalt Trackbed Component Materials' Properties and Performance, AREMA 2008.
[21] ANDO K, SUNAGA M, AOKI H, HAGA O. Development of Slab Tracks for Hokuriku Shinkansen Line. Quarterly Report of Rtri 2001;42:35–41.
[22] Georgios Michas. Slab track systems for high-speed railways. Royal Institute of Technology; 2012.
[23] Zhai W, Wang K, Cai C. Fundamentals of vehicle–track coupled dynamics. Vehicle System Dynamics 2009;47:1349–76.
[24] Lamprea-Pineda AC, Connolly DP, Hussein MFM. Beams on elastic foundations – A review of railway applications and solutions. Transportation Geotechnics 2022;33:100696.
[25] Zhai W, Sun X. A Detailed Model for Investigating Vertical Interaction between Railway Vehicle and Track. Vehicle System Dynamics 1994;23:603–15.
[26] Shan Y, Shu Y, Zhou S. Finite-infinite element coupled analysis on the influence of material parameters on the dynamic properties of transition zones. Construction and Building Materials 2017;148:548–58.
[27] Hall L. Simulations and analyses of train-induced ground vibrations in finite element models. Soil Dynamics and Earthquake Engineering 2003;23:403–13.
[28] Connolly D, Giannopoulos A, Fan W, Woodward PK, Forde MC. Optimising low acoustic impedance back-fill material wave barrier dimensions to shield structures from ground borne high speed rail vibrations. Construction and Building Materials 2013;44:557–64.
[29] Woodward PK, Laghrouche O, Mezher SB, Connolly DP. Application of Coupled Train-Track Modelling of Critical Speeds for High-Speed Trains using Three-Dimensional Non-Linear Finite Elements. International Journal of Railway Technology 2015;4:1–35.
[30] Shih JY, Thompson DJ, Zervos A. The effect of boundary conditions, model size and damping models in the finite element modelling of a moving load on a track/ground system. Soil Dynamics and Earthquake Engineering 2016;89:12–27.
[31] Shih JY, Thompson DJ, Zervos A. The influence of soil nonlinear properties on the track/ground vibration induced by trains running on soft ground. Transportation Geotechnics 2017;11:1–16.

[32] Powrie W, Yang LA, Clayton CRI. Stress changes in the ground below ballasted railway track during train passage. Proceedings of the Institution of Mechanical Engineers, Part F: Journal of Rail and Rapid Transit 2007;221:247–62.

[33] Varandas JN, Paixão A, Fortunato E, Hölscher P. A Numerical Study on the Stress Changes in the Ballast Due to Train Passages. Procedia Engineering 2016;143:1169–76.

[34] El Kacimi A, Woodward PK, Laghrouche O, Medero G. Time domain 3D finite element modelling of train-induced vibration at high speed. Computers & Structures 2013;118:66–73.

[35] Galvín P, Domínguez J. Analysis of ground motion due to moving surface loads induced by high-speed trains. Engineering Analysis with Boundary Elements 2007;31:931–41.

[36] Kouroussis G, Gazetas G, Anastasopoulos I, Conti C, Verlinden O. Discrete modelling of vertical track–soil coupling for vehicle–track dynamics. Soil Dynamics and Earthquake Engineering 2011;31:1711–23.

[37] Auersch L. The excitation of ground vibration by rail traffic: theory of vehicle–track–soil interaction and measurements on high-speed lines. Journal of Sound and Vibration 2005;284:103–32.

[38] O'Brien J, Rizos DC. A 3D BEM-FEM methodology for simulation of high speed train induced vibrations. Soil Dynamics and Earthquake Engineering 2005;25:289–301.

[39] Yang YB, Hung HH, Chang DW. Train-induced wave propagation in layered soils using finite/infinite element simulation. Soil Dynamics and Earthquake Engineering 2003;23:263–78.

[40] Alves Costa P, Calçada R, Silva Cardoso A, Bodare A. Influence of soil non-linearity on the dynamic response of high-speed railway tracks. Soil Dynamics and Earthquake Engineering 2010;30:221–35.

[41] Bian X, Chao C, Jin W, Chen Y. A 2.5D finite element approach for predicting ground vibrations generated by vertical track irregularities. J Zhejiang Univ Sci A 2011;12:885–94.

[42] Bian X, Chen Y, Hu T. Numerical simulation of high-speed train induced ground vibrations using 2.5D finite element approach. Sci China Ser G-Phys Mech Astron 2008;51:632–50.

[43] François S, Schevenels M, Galvín P, Lombaert G, Degrande G. A 2.5D coupled FE–BE methodology for the dynamic interaction between longitudinally invariant structures and a layered halfspace. Computer Methods in Applied Mechanics and Engineering 2010;199:1536–48.

[44] Alves Costa P, Calçada R, Silva Cardoso A. Track–ground vibrations induced by railway traffic: In-situ measurements and validation of a 2.5D FEM-BEM model. Soil Dynamics and Earthquake Engineering 2012;32:111–28.

[45] Charoenwong C, Connolly DP, Woodward PK, Galvín P, Alves Costa P. Analytical forecasting of long-term railway track settlement. Computers and Geotechnics 2022;143:104601.

[46] Charoenwong C, Connolly DP, Odolinski K, Alves Costa P, Galvín P, Smith A. The effect of rolling stock characteristics on differential railway track settlement: An engineering-economic model. Transportation Geotechnics 2022;37:100845.

[47] Kausel E. Wave propagation in anisotropic layered media. International Journal for Numerical Methods in Engineering 1986;23:1567–78.

[48] Kausel E. Thin-layer method: Formulation in the time domain. International Journal for Numerical Methods in Engineering 1994;37:927–41.

[49] Kausel E, Roësset JM. Stiffness matrices for layered soils. Bulletin of the Seismological Society of America 1981;71:1743–61.

[50] Bian X, Chen Y. An explicit time domain solution for ground stratum response to harmonic moving load. Acta Mech Mech Sinica 2006;22:469–78.

[51] Connolly DP, Dong K, Alves Costa P, Soares P, Woodward PK. High speed railway ground dynamics: a multi-model analysis. International Journal of Rail Transportation 2020;8:324–46.

[52] Fang M, Qiu Y, Rose JG, West RC, Ai C. Comparative analysis on dynamic behavior of two HMA railway substructures. J Mod Transport 2011;19:26–34.

[53] Fang M, Cerdas SF. Theoretical analysis on ground vibration attenuation using sub-track asphalt layer in high-speed rails. J Mod Transport 2015;23:214–9.

[54] Liu S, Chen X, Ma Y, Yang J, Cai D, Yang G. Modelling and in-situ measurement of dynamic behavior of asphalt supporting

layer in slab track system. Construction and Building Materials 2019;228:116776.

[55] Zhai W. Vehicle-track coupled dynamics: theory and applications. Singapore: Springer; 2020.

[56] TBT 3352-2014. PSD of ballastless track irregularities of high-speed railway, The National Railway Administration of China: 2014.

[57] Chen G, Zhai W. Numerical Simulation of the Stochastic Process of Railway Track Irregularities. Journal of Southwest Jiaotong University 1999:13–7.

[58] TB 10082-2017. Code for Design of Railway Track, The National Railway Administration of China: 2017.

[59] Zeng Z, Shen S, Li P, Abdulmumin AS, Wang W. Experimental study on evolution of mechanical properties of CRTS III ballastless slab track under fatigue load. Construction and Building Materials 2019;210:639–49.

[60] Gao L, Zhao L, Qu C, Cai X. Analysis on Design Scheme of CRTSIII Slab Track Structure on Roadbed. Journal of Tongji University(Natural Science) 2013;41:848–55.

[61] Liu J, Gu Y, Du Y. Consistent viscous-spring artificial boundaries and viscous-spring boundary elements. Chinese Journal of Geotechnical Engineering 2006:1070–5.

[62] Chen M, Sun Y, Zhu S, Zhai W. Dynamic performance comparison of different types of ballastless tracks using vehicle-track-subgrade coupled dynamics model. Engineering Structures 2021;249:113390.

[63] Chen M, Sun Y, Zhai W. High efficient dynamic analysis of vehicle–track–subgrade vertical interaction based on Green function method. Vehicle System Dynamics 2020;58:1076–100.

[64] Zhang R. Exploration of Design Technique on Substructure for 400km/h High-speed Railway and 40t Axle-load Heavy Haul Railway. Southwest Jiaotong University, 2017.

[65] Luo Q, Zhang R, Xie H, Tian D. Structural Analysis and Key Parameter of Ballastless Track Subgrade for 400km·h-1 High-Speed Railway. China Railway Science 2020;41:34–44.

[66] Liu S, Chen X, Yang J, Cai D, Yang G. Numerical study and in-situ measurement of temperature features of asphalt supporting layer in slab track system. Construction and Building Materials 2020;233:117343.

[67] Ali Y, Irfan M, Ahmed S, Khanzada S, Mahmood T. Investigation of factors affecting dynamic modulus and phase angle of various asphalt concrete mixtures. Mater Struct 2016;49:857–68.

[68] Zhu H, Sun L, Yang J, Chen Z, Gu W. Developing Master Curves and Predicting Dynamic Modulus of Polymer-Modified Asphalt Mixtures. J Mater Civ Eng 2011;23:131–7.

[69] Dong Z, Ma X. Analytical solutions of asphalt pavement responses under moving loads with arbitrary non-uniform tire contact pressure and irregular tire imprint. Road Materials and Pavement Design 2018;19:1887–903.

[70] Ferry JD, Grandine LD, Fitzgerald ER. The Relaxation Distribution Function of Polyisobutylene in the Transition from Rubber-Like to Glass-Like Behavior. Journal of Applied Physics 1953;24:911–6.

[71] Zhang Y, Punnett L, McEnany GP, Gore R. Contributing influences of work environment on sleep quantity and quality of nursing assistants in long-term care facilities: A cross-sectional study. Geriatric Nursing 2016;37:13–8.

[72] Liu S, Chen X, Ma Y, Yang J, Cai D, Yang G. Modelling and in-situ measurement of dynamic behavior of asphalt supporting layer in slab track system. Construction and Building Materials 2019;228:116776.

[73] Xu G. Temperature features of the asphalt concrete waterproofing layer on high-speed railway in cold regions. Construction and Building Materials 2021:11.

[74] Liu G, Luo Q, Zhang L, Chen H, Chen J. Analysis on the dynamic stress characteristics of the unballsted track subgrade under train loading. Journal of the China Railway Society 2013;35:86–93.

[75] Ye Y-S, Cai D, Wei S, Yu L, Shi Y, Wang L. Distribution Characteristics and Analytical Method of Dynamic Stress on Subgrade of Ballastless Track for High-Speed Railway. China Railway Science 2020;41:1–9.

[76] Ye Q, Luo Q, Feng G, Wang T, Xie H. Stress distribution in roadbeds of slab tracks with longitudinal discontinuities. Rail Eng Science 2022.

[77] Huang YH. KENTRACK, a computer program for hot-mix asphalt and conventional ballast railway trackbeds. NAPA PUBLICATION ; 1984.

[78] Wang T, Luo Q, Liu J, Liu G, Xie H. Method for slab track substructure design at a speed of 400 km/h. Transportation

Geotechnics 2020;24:100391.
[79] Zhang Q, Han Z, Lv B. Structural Analysis and Design Method for Subgrade Bed of High-speed Railway. China Railway Science 2005:55–9.
[80] Sun T. Research on Influence of Moisture Content on Test Index of Subgrade Compaction. Shijiazhuang Tiedao University, 2020.